

Chemistry in the High expansion-velocity C-rich evolved star AFGL 2233 $\star \star \star$

Isotopic ratios, peculiarities and evolutionary status.

G. Quintana-Lacaci¹, M. Agúndez¹, L. Velilla-Prieto¹, J. Alcolea², A. Castro-Carrizo³, J.P. Fonfría¹, and J. Cernicharo¹

¹ Department of Molecular Astrophysics, Instituto de Física Fundamental (IFF-CSIC), C/ Serrano 123, 28006 Madrid, Spain

² Observatorio Astronómico Nacional (IGN), Alfonso XII No. 3, 28014 Madrid, Spain

³ Institut de Radioastronomie Millimétrique, 300 rue de la Piscine, 38406 Saint Martin d'Herès, France

Received September 15, 1996; accepted March 16, 1997

ABSTRACT

Context. High expansion velocity carbon stars (HVCs) are a rare class of evolved stars whose circumstellar envelope (CSE) combine a C-rich chemistry with unusually high expansion velocities that are typical in O-rich massive evolved stars. These objects, in particular AFGL 2233, have been proposed to be high-mass evolved objects with an exhausted hot-bottom burning. Studying their chemistry is essential to understand the nature of these objects.

Aims. We aim to characterize the chemical composition and isotopic ratios of the circumstellar envelope of AFGL 2233. We also investigate the origin of several chemical peculiarities observed in this source, including the presence of nitrogen- and oxygen-bearing species in a C-rich environment.

Methods. We carried out a complete line survey at 3 mm and 1 mm using the IRAM 30m telescope, complemented by Herschel/HIFI FIR observations and interferometric maps of species such as SiO, C₂H or HCN. The molecular emission was analyzed using rotational diagrams and radiative transfer modeling under the LVG approximation. Column densities and fractional abundances were derived for over 30 molecular species, including isotopologues. The results were compared with those of other well-studied evolved stars.

Results. The revised Gaia DR3 distance of 1.236 kpc implies a luminosity of $\sim 2 \times 10^4 L_\odot$ consistent with an initial mass of 4.5–9 M_\odot . The molecular inventory confirms a C-rich chemistry, but also reveals unusually high abundances of NH₃, H₂O, and SiN. The derived isotopic ratios show significant variations across different species, with ¹²C/¹³C ranging from 7 to 55, which reflects opacity effects in some cases. The C₂H/C₄H ratio is abnormally high compare with C-rich AGB stars. The presence of SiN and the high NH₃ abundance can either point to a N-enrichment or the influence of a companion.

Conclusions. AFGL 2233 is likely a high-mass AGB or super-AGB star that experienced hot-bottom burning in the past. Its current C-rich chemistry, combined with signs of N-enrichment and the presence of O-bearing species, suggests a complex evolutionary history. The observed chemical anomalies may result from a combination of nucleosynthesis and other chemical processing effects such as shock-induced chemistry and binary influence.

Key words. circumstellar envelopes – molecular spectroscopy – isotopic ratios – evolved stars – AFGL 2233

1. Introduction

The role of the evolved stars is essential for the chemical evolution of the Galaxy (Habing & Olofsson 2003). The elements synthesized in their interiors are transported to the photosphere during the late stages of stellar evolution, and subsequently expelled into the interstellar medium (ISM) through intense mass-loss episodes. This process, which is particularly efficient during the Asymptotic Giant Branch (AGB) and Red Supergiant (RSG) phases, leads to the formation of extended circumstellar envelopes (CSEs) where a rich molecular chemistry develops. The chemical composition of these envelopes is mainly deter-

mined by the nucleosynthesis processes that have taken place in the stellar interior, as the Hot Bottom Burning (HBB), and by the efficiency of mixing mechanisms such as the third dredge-up.

In the case of intermediate-mass stars ($M_{\text{init}} \sim 1.5\text{--}4 M_\odot$), the third dredge-up (TDU) leads to a C-rich photosphere (C/O > 1), while in more massive stars ($M_{\text{init}} \gtrsim 4\text{--}8 M_\odot$), the activation of HBB prevents the formation of carbon stars by converting ¹²C into ¹⁴N in the stellar core. As a result, C-rich envelopes are typically associated with low- and intermediate-mass AGB stars. In addition, due to their luminosities and due to the radiation pressure acting as the main driver of mass ejection, the expansion velocities are lower in C-rich stars ($v_{\text{exp}} \sim 10\text{--}20 \text{ km s}^{-1}$, e.g. Massalkhi et al. 2019) than in massive O-rich stars ($v_{\text{exp}} \sim 30\text{--}40 \text{ km s}^{-1}$, Quintana-Lacaci et al. 2007). However, a small group of evolved stars challenges this paradigm: the so-called High expansion Velocity Carbon stars (HVCs), which combine a C-rich chemistry with unusually high expansion velocities ($v_{\text{exp}} \gtrsim 25 \text{ km s}^{-1}$). These objects are rare and poorly understood, and their nature remains uncertain.

\star This work is based on observations carried out under project numbers V016 and V074 with the IRAM Plateau de Bure Interferometer, and 050-19 with the IRAM 30m telescope. IRAM is supported by INSU/CNRS (France), MPG (Germany) and IGN (Spain).

$\star\star$ *Herschel* is an ESA space observatory with science instruments provided by European-led Principal Investigator consortia and with important participation from NASA. *HIFI* is the Herschel HeterodyneInstrument for the Far Infrared.

AFGL 2233 is one of these HVC stars. Its CO line profiles reveal a terminal expansion velocity of $\sim 32 \text{ km s}^{-1}$, significantly higher than the average for C-rich AGB stars (Loup et al. 1993). Its infrared spectrum shows the characteristic $11 \mu\text{m}$ SiC feature Yang et al. (2004), and previous studies have reported strong emission from molecules such as HCN (Likkel & Miao 1996) and high abundances of C₂H (Fuente et al. 1998). These properties, together with its long pulsation period ($P \sim 687$ days), initially suggested that AFGL 2233 could be a massive object with a C-rich envelope, possibly formed after the exhaustion of HBB (Quintana-Lacaci et al. 2019).

Quintana-Lacaci et al. (2019) assumed a distance to AFGL 2233 4.16 kpc (from Gaia DR2), leading to a derived luminosity of $\log(L/L_\odot) \sim 5.4$ and a total envelope mass of $\sim 1.7 M_\odot$, values consistent with a massive origin. However, the recent release of Gaia DR3 has provided a revised parallax for this source, yielding a Bayesian distance of 1.236 kpc (see Sect. 3).

In this paper, we first revisited the luminosity, density and temperature profiles with this new distance estimate. After this update, we present a detailed chemical analysis of AFGL 2233 based on a complete line survey at 3 mm and 1 mm obtained with the IRAM 30m telescope, complemented by HIFI observations from the Herschel Space Observatory and interferometric maps of different species. This study provides new constraints on the physical and chemical properties of AFGL 2233. Our goals are to characterize the molecular content and isotopic composition of the envelope, to investigate the origin of the observed chemical anomalies, and to understand the evolutionary status of AFGL 2233 in the context of massive AGB and super-AGB stars.

2. Observations

2.1. HIFI Data

AFGL 2233 was observed in April 2013 using the Heterodyne Instrument for the Far Infrared (HIFI, de Graauw et al. 2010) onboard the HSO (Pilbratt et al. 2010). We observed bands 1b, 2a, 5a, 4b, 7b to cover transitions from species such as H₂O, CO, SiO, NH₃ or H¹³CN. The values of the system temperature were $T_{\text{sys}} \sim 90 - 390 \text{ K}$ for bands 1 to 4, and 830 K and 1240 K for bands 5a and 7b respectively (see table 1).

Observational procedure was similar to that used in the HIFISTARS programme (P.I. V. Bujarrabal). This procedure is fully described in Alcolea et al. (2013); here we briefly summarize its main characteristics. The observations were performed using the two orthogonal linearly polarized receivers available at each band, named H and V (horizontal and vertical) after their mutually perpendicular orientations. The receivers worked in double side-band mode (DSB), providing an instantaneous frequency coverage of 4 plus 4 GHz for bands 1 to 5, and 2.6 plus 2.6 GHz for band 7. The observations were all performed in the dual-beam switching (DBS) mode, alternating between the ON source position and two OFF reference positions located 3 arc-minutes away at either side of the science target (see Roelfsema et al. 2012, for additional details). This DBS subtraction procedure worked well except for band 7, where strong ripples (generated by electrical standing waves) are often found in the averaged spectra, especially in the case of the V-receiver. The data shown here were taken using the wide-band spectrometer (WBS), with an effective spectral resolution slightly varying across the band, with a mean value of 1.1 MHz. The data were retrieved from the Herschel Science Archive and were reprocessed

using a modified version of the standard HIFI pipeline using HIPE¹, providing as final result individual ON-OFF elementary integrations without performing the final time-averaging. Later on, these spectra were exported to CLASS² using the hiClass tool within HIPE for further processing. Time-averaging was also performed in CLASS, as well as baseline removal, and combination of the results from the H and V receivers.

In general, the data presented no problems and did not need a lot of flagging, except for band 7, for which a semiautomated procedure was designed in CLASS to detect and remove the sub-scans in which the ripples were more severe. The application of this procedure normally results in the rejection of 30% to 50% of the non-averaged spectra, which produces a final spectrum slightly noisier, but with a more reliable baseline.

The original data were oversampled to a uniform channel spacing of 0.5 MHz, but we smoothed all spectra down to a velocity resolution of about 1 km s^{-1} . The data were re-calibrated into (Rayleigh-Jeans equivalent) main-beam temperatures (T_{mb}) adopting the latest available values for the telescope and main beam efficiencies (Roelfsema et al. 2012). In all cases we assumed a side-band gain ratio of one.

2.2. IRAM 30m data

We used the IRAM 30m radiotelescope to obtain a complete line survey at 3 mm and 1 mm for the HVC AFGL 2233. We observed AFGL 2233 at the position coordinates (J2000) $18^{\text{h}}42^{\text{m}}24\overset{\text{s}}{.}680 - 02^{\circ}17'25\overset{\text{s}}{.}200$ with an $v_{\text{LSR}} = 2.80 \text{ km/s}$. The observations were obtained during September and November 2019. We used the EMIR receiver, simultaneously using the receivers E090 and E230 with a bandwidth of 4 GHz. We used 7 different setups to cover the atmospheric windows at 3 mm and 7 setups at 1 mm covering both polarizations. For each setup, we observed every setup twice, introducing a frequency shift of 50 MHz between the two observations for easing the identification of spectral features arising from the image band. In total each setup was observed for 3h ($= 2 \times 1.5 \text{ h}$). We used the wobbler switching mode to minimize the ripples in the baselines. The system temperatures during the observations were in the range 70–280 K for the E090 receiver (3 mm receiver band) and between 200 and 425 K for the E230 receiver (1.3 mm band). The weather conditions during the observations were good with an amount of precipitable water vapor ranging between 2 and 6 mm.

The backends used were WILMA (spectral resolution 2 MHz) and the FFT with a spectral resolution of 0.195 MHz. Since the profiles of AFGL 2233 are known to be relatively wide the spectra could be smoothed to increase the SNR.

The pointing correction was checked frequently and, therefore, we expect pointing errors of $\sim 3''$. Focus was checked at the beginning of the observing runs, and after changes in the temperature of the telescope structure (i.e. during dusk and dawn). The telescope beam size at 3 mm is $21\text{--}29''$ and $9\text{--}13''$ at 1 mm. The Atmospheric Transmission Model (ATM) is adopted at the IRAM 30 m (Cernicharo 1985; Pardo et al. 2001). The data presented are calibrated in antenna temperature (T_A^*). The calibra-

¹ HIPE is a joint development by the Herschel Science Ground Segment Consortium, consisting of ESA, the NASA Herschel Science Center, and the HIFI, PACS, and SPIRE consortia. Visit <https://www.cosmos.esa.int/web/herschel/hipe-download> for additional information.

² CLASS is part of the GILDAS software package, developed and maintained by IRAM, LAOG/Univ. de Grenoble, LAB/Obs. de Bordeaux, and LERMA/Obs. de Paris. For more details, see <http://www.iram.fr/IRAMFR/GILDAS>

Table 1: Main parameters of the HIFI observations.

Herschel OBSID	Obs. date yr:mo:day	Durat. (s)	Sky frequency coverage LSB (GHz)	Sky frequency coverage USB (GHz)	T _{sys} (K)	HIFI band	HPBW (")	Cal. uncer
1342269367	2013:04:04	1830	556.44–560.57	568.42–572.56	88	1b	39.6	15%
1342269369	2013:04:04	3421	645.45–649.59	657.44–661.58	122	2a	34.3	15%
1342269370	2013:04:04	1350	678.36–682.50	690.35–694.48	132	2a	32.7	15%
1342269377	2013:04:04	3720	1149.61–1153.75	1161.60–1165.73	831	5a	19.4	20%
1342269400	2013:04:04	2258	1099.04–1103.17	1111.02–1115.16	394	5a	20.3	20%
1342269402	2013:04:04	2361	1833.41–1835.98	1840.66–1843.23	1245	7b	12.3	30%

tion error is expected to be 10% at 3 mm and 30% at 1 mm. The data were processed using the GILDAS package³. Both polarization were averaged, since no changes were observed in the line intensities along the line survey. Baselines were subtracted using only first order polynomials.

2.3. IRAM PdBI data

Observations towards AFGL 2233 were performed with the former Plateau de Bure Interferometer (with 6 antennas, early version of the NOEMA interferometer). Three short tracks were obtained in 6Cq configuration in November 2011 (project name V016), and one in 6Bq configuration in March 2012 (project name V074). Single sideband receivers were tuned at 88.630 GHz to observe the frequency interval from 87.83 to 91.43 GHz, with different spectral resolutions, from 1 to 8 km s⁻¹. Four intervals were obtained with the highest spectral resolution: [89.15 - 89.23], [88.60 - 88.67], [87.5 - 87.6] and [86.8 - 86.9] GHz. All observations were performed in good conditions, with 1749+096 and 1827+062 as phase calibrators. Data calibration was straightforward for all the tracks, resulting in uncertainties below 5% and 20 degrees for amplitudes and phases. The absolute flux calibration was made by using the main reference at the observatory, MWC 349, for which a flux of 1.1 Jy at 88.630 GHz was adopted. Uncertainties in the absolute flux calibration in 2011-2012 were below 10% at 3 mm. The calibration and data analysis were performed in the standard way by using the GILDAS software package.

We were able to detect the emission from species as H¹³CN 1 – 0, SiO 5 – 4, CCH 1 – 0, HC₅N 33 – 32, H¹³CCCN 10 – 9, HCN 1 – 0, C₃N 9 – 8. The obtained total integrated emission spectrum is presented in Fig. 1, and the channel maps are shown in Appendix C.

3. 2019 results revisited. Gaia DR3.

Since the publication of Quintana-Lacaci et al. (2019) a new Gaia data release has been published (Gaia Collaboration et al. 2023). The new measurement of the parallax of AFGL 2233 is better constrained, being the error significantly lower than that provided in GAIA DR2 (Gaia Collaboration et al. 2016).

In Quintana-Lacaci et al. (2019) we assumed a distance of 4.16 Kpc (from Yuasa et al. 1999). This estimate was derived based on radial velocities and its result was uncertain. Also Gaia DR2 data had a very large error, similar to the derived distance itself, but the derived distance estimate was similar to that from Yuasa et al. (1999). Due to this, Yuasa et al. (1999) estimate was adopted by Quintana-Lacaci et al. (2019). However, the new Bayesian (GSP-Phot-Aeneas, Andrae et al. 2023) distance

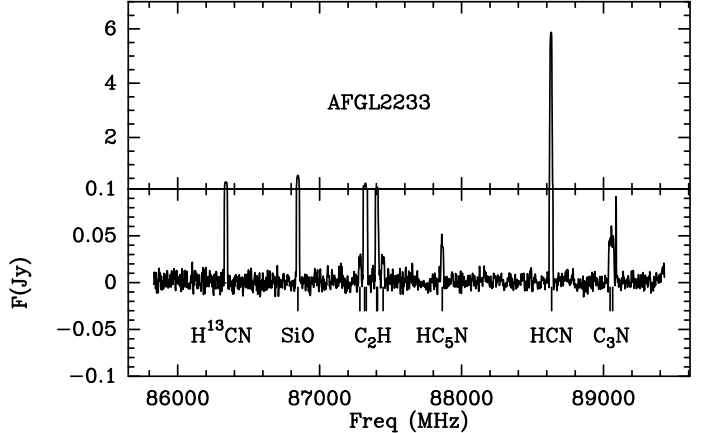


Fig. 1: Spectra of the integrated flux obtained with IRAM PdBI towards AFGL 2233.

of GAIA DR3 is much better constrained. This latter estimate is 1.236 Kpc (with a confidence interval ranging from 1.165 to 1.431 pc). While the distance determination is still unsure for Red giant stars, we have revisited the results of the cited paper with the new distance. It is worth noting, in any case, that the column densities derived in this work are independent of the distance.

The methodology applied is exactly the same presented in Quintana-Lacaci et al. (2019).

3.1. Spectral energy distribution (SED).

As in Quintana-Lacaci et al. (2019) we found that, to be able to properly fit the SED of AFGL 2233, we needed two independent black bodies. We found that the best fit – following a χ^2 methodology – is obtained for a $T_{\star} = 900$ K and $r_{\star} = 3.1 \times 10^{14}$ cm and $T_{\text{gas}} = 300$ K and $r_{\text{gas}} = 10^{15}$ cm (see Fig. 2).

The luminosity derived for this new distance is $\log(L/L_{\odot})=4.3$ (instead of $\log(L/L_{\odot})=5.4$, Quintana-Lacaci et al. 2019). This suggests, according to the evolutionary models by Meynet & Maeder (2003) or Girardi et al. (2000) that AFGL 2233 would have an initial mass, M_{init} between $4.5M_{\odot}$ and $9M_{\odot}$ depending on different factors such as metallicity or rotation. We conclude that this object probably is a RSG or a super-AGB.

3.2. Molecular emission model.

Following the same method as in Quintana-Lacaci et al. (2019) – modeling the CO emission adopting an LVG approximation, assuming a constant mass loss and expansion velocity, and a temperature following $T(r) = T_{16}(r/10^{16})^{\alpha_t} + T_{\text{min}}$ within a certain

³ See <http://www.iram.fr/IRAMFR/GILDAS> for more information about the GILDAS software.

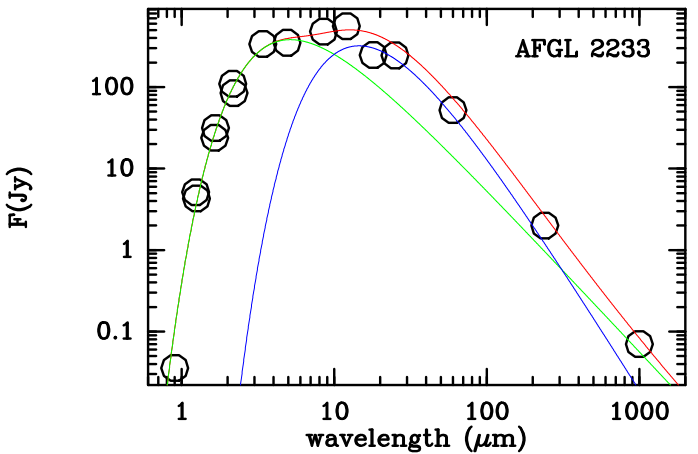


Fig. 2: SED fitting obtained with the new distance estimate for AFGL 2233. Green and blue curves correspond to the two components, and the red curve to the sum of both components.

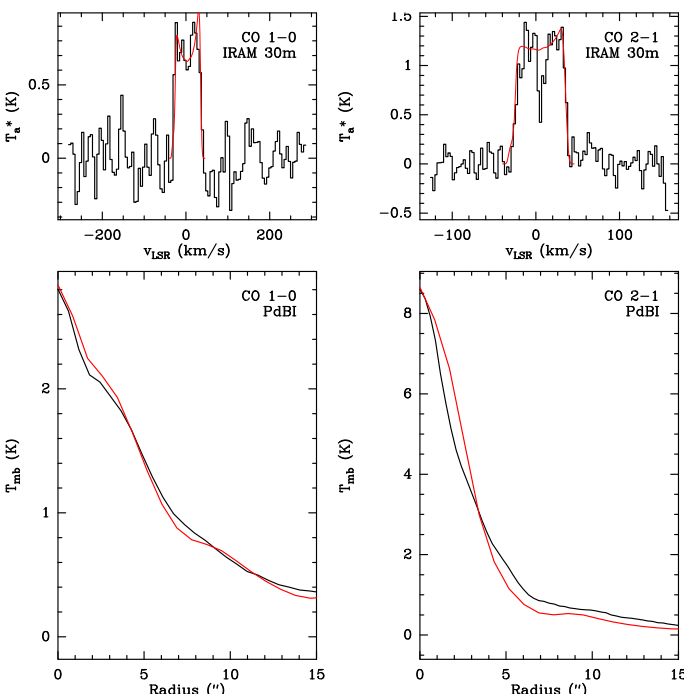


Fig. 3: Top-left: CO $J = 1 - 0$ line profile obtained with the IRAM 30m telescope for AFGL 2233. Top-right: CO $J = 2 - 1$ line profile obtained with the IRAM 30m telescope for AFGL 2233. Bottom-left: Azimuthally averaged profile of the CO $J = 1 - 0$ molecular emission of the central velocity channel obtained towards AFGL 2233 with PdBI. Bottom-right: Azimuthally averaged profile of the CO $J = 2 - 1$ molecular emission of the central velocity channel obtained towards AFGL 2233 with PdBI. The black lines correspond to the observations and the red lines to the results of the model.

region (or shell) –, and assuming the new distance, we fitted both the single-dish CO $J = 1 - 0$ and $J = 2 - 1$ observations obtained at the IRAM 30m radiotelescope and the azimuthal averaged profiles of the interferometric maps obtained with IRAM PdBI for the same transitions. The results are listed in the Table 2.

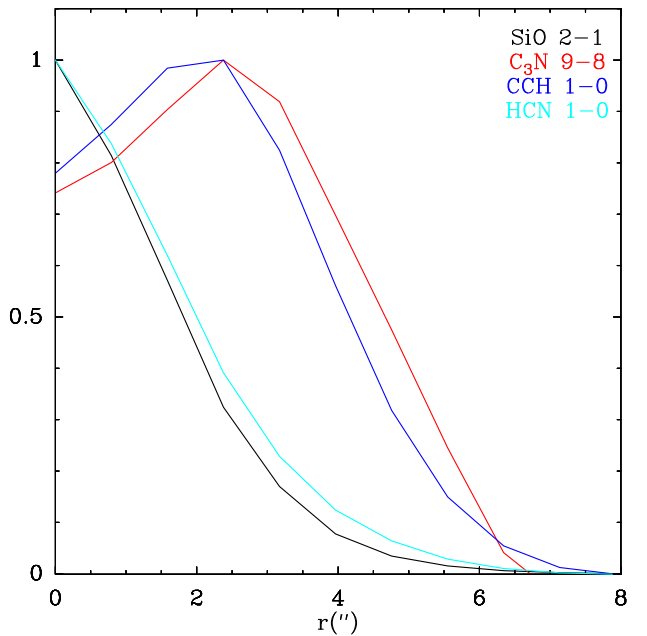


Fig. 4: Azimuthal averaged intensity of the different transitions observed with PdBI for the central velocity channel, normalized to its maximum intensity.

The total circumstellar mass derived from the fitting of these observations, for the new distance estimate, is $0.19 M_{\odot}$. This value, for an outer radius of 7×10^{17} cm results in a column density $N_{\text{H}_2} = 7.4 \times 10^{19}$ cm $^{-2}$ for CO.

4. Results

In this section we will present the results obtained from the observations presented above.

4.1. Structure of the ejecta

In addition to the CO $J = 1 - 0$ and $J = 2 - 1$ interferometric maps obtained by Quintana-Lacaci et al. (2019) we have maps of SiO $J = 2 - 1$, C₂H $N = 1 - 0$, HCN $J = 1 - 0$, C₃N $N = 9 - 8$, H¹³CN $J = 1 - 0$ and HC₅N $J = 9 - 8$ (see Figs C.1–C.8). These maps allowed us to have an estimate of the extent of the different line emissions. All these maps confirm the spherical structure observed in the CO maps. The emission from C₂H and C₃N shows clear hints of a hollow shell, however the size of the inner hole cannot be resolved. The size estimated for the different species is presented in Table 3. This estimate was obtained from azimuthal averaged maps of the central channels of the different molecular lines (see Fig. 4).

To estimate the H₂ column density associated with the molecules found in the inner regions, relative to the full extent of CO, we used the interferometric maps presented here.

We estimated the total mass within the values of R_{out} obtained, and given this size we estimated the value of N_{H_2} associated with each species. In particular, we integrated the density profile obtained for CO and constrained that integration to the radii where each species are located from the interferometric maps (i.e. $N_{\text{H}_2}(\text{mol}) = \int_{R_{\text{in}}}^{R_{\text{out}}} n(r) dr$). These estimates are presented in Table 3.

The H₂ column density associated with the C₂H emitting region is an upper limit as long as the inner hole for this species

Table 2: Best fit parameters for AFGL 2233.

Shell	R_{in} (cm)	R_{out} (cm)	$\dot{M}(M_{\odot} \text{ yr}^{-1})$	V_{exp} (km s $^{-1}$)	T_{16} (K)	α_t	T_{min} (K)
1	1×10^{14}	5×10^{16}	1.8×10^{-5}	32	50	0.6	2.73
2	5×10^{16}	9×10^{16}	2.6×10^{-5}	32	150	0.6	2.73
3	9×10^{16}	3×10^{17}	2.1×10^{-5}	32	500	0.6	2.73
4	3×10^{17}	7×10^{17}	3.2×10^{-5}	32	450	0.6	2.73

Table 3: Extent of the emission observed for different species and H₂ column density within these radii.

Molecule	R_{out} (cm)	N_{H_2} (cm $^{-2}$)	Comment
CO	7×10^{17}	7.4×10^{19}	
HCN	7.8×10^{16}	5.0×10^{20}	
SiO	7.0×10^{16}	5.5×10^{20}	
C ₃ N	1.1×10^{17}	$< 3.7 \times 10^{20}$	Hollow shell structure.
C ₂ H	1.1×10^{17}	$< 3.7 \times 10^{20}$	"

is not resolved. As the HPBW is $4''.25 \times 2''.78$, we would set as an upper limit to the size of this hole the same as the HPBW (i.e. $\sim 3''.4 = 3.2 \times 10^{16}$ cm). This would lead to an upper limit $N_{\text{H}_2} < 1.4 \times 10^{20}$ for C₂H. In a similar way, the emission from C₃N has also been observed to have an inner hole, which is not resolved in our case (Agúndez et al. 2017). In any case, it is worth noting that the impact of the inner radius in the estimate of column density is low. This is particularly relevant for species presenting inner holes as C₂H or C₃N. In those particular cases, varying R_{in} from 10^{14} cm to 10^{16} cm only modifies N_{H_2} by a 8%.

4.2. Line identification

The IRAM-30m data showed a rich spectrum. We identified more than 150 spectral features arising from 31 molecular species (see Table 4).

The complete spectra obtained in the 3 mm and 1 mm bands is shown in Sect.D. The EMIR receiver used for the observations provides a sideband rejection ratio exceeding 13 dB, which ensures that only the most intense spectral features exhibit counterparts from the image band. In our particular case, by comparing the results from the two observations of each setup, which differ by 50 MHz in their tuning, we conclude that there is no image-band contribution in the spectra.

Spectral line identification was conducted using the internal database of the MADEX radiative transfer code (Cernicharo 2012).

Table A.1 list all the molecular transitions detected in the 3 mm and 1 mm spectral scans. For each transition, we report the velocity-integrated intensity, peak intensity, and the rms noise level. As a result of the large expansion velocities present in AFGL 2233, the hyperfine structure of species such as CN is not spectrally resolved. Consequently, the reported integrated intensities for these species correspond to the sum over all hyperfine components.

4.3. Abundance and temperature estimate

In general we have used the method of the rotational diagrams (Goldsmith & Langer 1999). In most of the cases a single component was enough to fit the data obtained. However, in certain cases, in which the presence of two components was clearly observed in the rotational diagrams, we fitted both components

Table 4: Molecular species detected and number of molecular transitions observed in the different sets of data presented.

Species	lines	Species	lines
CO	5	¹³ CO	2
HCN	2	HNC	2
HC ₃ N	12	HC ¹³ CCN	2
H ¹³ CN	3	H ¹³ CCCN	2
HCC ¹³ CN	3	HC ₅ N	15
HC ₇ N	1	C ₃ N	6
CN	5	¹³ CN	5
C ₄ H	20	H ₂ O	2
CCS	4	NH ₃	1
CCH	16	C ¹³ CH	1
SiO	4	²⁹ SiO	3
SiS	7	³⁰ SiO	3
SiN	2	¹³ CS	2
CH ₃ CN	4	C ³⁴ S	2
CS	2	SiC ₂	23
C ³³ S	2		

which allowed us to obtain a column density and rotational temperature for each of them. These results are presented in Table 5. In the cases in which we fitted two components the density and temperature are presented as N^C & T_{rot}^C and N^H & T_{rot}^H for the cold and hot components respectively. When only a single component was fitted, it was labeled as the cold component.

To obtain an estimate of the total abundance of each species we used that $X_{\text{mol}} = N_{\text{mol}}/N_{\text{H}_2}$. Since we have an estimate of N_{H_2} for the outer species and the innermost ones, and given that $N_{\text{mol}} = N_{\text{mol}}^C + N_{\text{mol}}^H$ we could have an estimate of the fractional abundances of the different species. These results are also shown in Table 5.

In particular we adopted that CO and ¹³CO would have similar N_{H_2} , Si-bearing species and CS would have a value of N_{H_2} similar to SiO, HCN and H¹³CN also would present similar values of N_{H_2} , and the carbon chains would have a similar N_{H_2} as C₂H and C₃N. The emission observed from HC₅N 9–8 is relatively weak; its real extent can be assumed to be smaller. Therefore, we assumed that its extent is similar to that of C₂H (or C₃N). Previous results, as those presented by Agúndez et al. (2017), show that these are reasonable assumptions.

The results for the different species are commented in the following sub-sections.

4.3.1. CO & ¹³CO.

In the case of CO we count with high excitation lines, and thus we were able to fit both a hot and a cold component. The hot component has a column density of 1.4×10^{14} cm $^{-2}$ and a T_{rot} of 413 K, while the cold one has a column density of 2.46×10^{17} cm $^{-2}$ and $T_{\text{rot}} = 16$ K. In the case of ¹³CO only two

Table 5: Column densities and rotational temperatures.

Molecule	N^C (cm $^{-2}$)	T_{rot}^C (K)	N^H (cm $^{-2}$)	T_{rot}^H (K)	$\langle X \rangle$	N. Lines fit	N_{H_2}	Comment
CO	$2.4(6) 10^{17}$	16(3)	$1.4(4) 10^{14}$	413(124)	$3.6 10^{-4}$	5	CO	
^{13}CO	$4.4(2) 10^{15}$	7.8(2)	—	—	$6.8 10^{-6}$	2	CO	
HCN	$2.80(3) 10^{14}$	51(2)	—	—	$5.6 10^{-7}$	2	HCN	Intense $J = 1 - 0$
H^{13}CN	$8.79(1) 10^{13}$	8.7(0)	$1.6(1) 10^{13}$	20(1)	$2.1 10^{-7}$	3	HCN	
HC_3N	$2.8(6) 10^{14}$	22(4)	$6(3) 10^{12}$	75(18)	$7.6 10^{-7}$	12	C_3N	
H^{13}CCCN	$4.9(8) 10^{12}$	12(1)	—	—	$1.4 10^{-8}$	3	C_3N	
HC_5N	$3.2(3) 10^{13}$	28(1)	$1.5(4) 10^{12}$	149(53)	$8.9 10^{-8}$	15	C_3N	
SiO	$1.89(6) 10^{14}$	14.3(6)	$3.0(1) 10^{13}$	40(1)	$4.0 10^{-7}$	4	SiO	
^{29}SiO	$1.38(2) 10^{12}$	13.3(3)	$3.0(5) 10^{12}$	38(5)	$3.1 10^{-8}$	3	SiO	
^{30}SiO	$1.04(1) 10^{13}$	14.6(3)	$4.8(8) 10^{12}$	23(2)	$2.8 10^{-8}$	3	SiO	
SiS	$1.14(6) 10^{14}$	50(4)	—	—	$2.1 10^{-7}$	7	SiO	High excitation levels
CS	$1.13(4) 10^{14}$	14.8(0)	—	—	$2.1 10^{-6}$	2	SiO	
^{13}CS	$2.06(7) 10^{13}$	13.5(0.8)	—	—	$3.8 10^{-8}$	2	SiO	
C^{34}S	$6.87(3) 10^{13}$	16.3(1)	—	—	$1.3 10^{-7}$	2	SiO	
SiC_2	$2.7(2) 10^{14}$	23(2)	$1.5(8) 10^{13}$	204(218)	$7.7 10^{-7}$	23	C_2H	
HNC	$5.10(4) 10^{13}$	7.2(1)	—	—	$>1.4 10^{-7}$	2	C_2H	
CCS	$2.5(9) 10^{13}$	15(4)	—	—	$>6.7 10^{-8}$	4	C_2H	
CCH	$4.0(1) 10^{15}$	16(1)	—	—	$>1.1 10^{-5}$	10	C_2H	
C_4H^a	$6.6(2) 10^{14}$	46(2)	—	—	$>1.8 10^{-7}$	8	C_2H	
C_4H^b	$7.4(4) 10^{14}$	50(3)	—	—	$>2.0 10^{-7}$	8	C_2H	
CN	$1.7(3) 10^{13}$	4.2(0.4)	—	—	$>1.3 10^{-5}$	3	C_2H	
CCCN	$5.6(6) 10^{13}$	29(4)	—	—	$>1.7 10^{-7}$	3	C_2H	
$^{13}\text{CCCN}$	$8 10^{12}$	29	—	—	$>2.2 10^{-8}$	1	C_2H	LTE. $T_{\text{rot}}(\text{C}_3\text{N})$ assumed

transitions where available from our data and a single component was fitted ($N = 4.4 10^{15} \text{ cm}^{-2}$, $T_{\text{rot}} = 7.8 \text{ K}$). The temperature obtained for ^{13}CO is significantly lower than that obtained for the cold component of ^{12}CO . However, if we just only take into account for the ^{12}CO fitting up $J = 1 - 0$ & $2 - 1$, the rotational temperature derived is $\sim 10 \text{ K}$ while the column density remains the same. This suggests that the value of T_{rot} derived is artificially low, but the column density is reliable.

The column density derived via our LVG modeling (see Sect. 3.2) is $3.4 \times 10^{20} \text{ cm}^{-2}$ and thus the fractional abundances with respect to H_2 obtained are 7×10^{-4} and 1.3×10^{-5} respectively for CO and ^{13}CO .

The value of the CO fractional abundance (3×10^{-4}) was already an input in our LVG model (Sect. 3.2) and deriving it here – from the rotational diagrams and the density structure obtained above – works as a test of the validity of the approximations made.

The optical depths obtained in the rotational diagrams for the different CO transitions range between 0.15 and 2 for the low-excitation lines (much lower values are obtained for the high-excitation lines). These values are taken into account and corrected in our rotational diagram fitting (see Quintana-Lacaci et al. 2016).

4.3.2. HCN, HC_3N , CN and HNC

The particularly high intensity of the HCN 1 – 0 line has been already reported by Likkel & Miao (1996). These authors suggested that this high intensity could be due to an abnormally high HCN abundance. The latter case is associated by these authors to a N-enrichment related with the massive nature of this object.

We have tried to model the HCN line profiles as well as the HCN $J = 1 - 0$ interferometric maps using a LVG approach.

However, the intensity of this transition seemed too intense, suggesting indeed the presence of another contribution we could not model. The fitting revealed that our synthetic profiles lacked on emission for the $J = 1 - 0$ emission in the inner regions of the CSE ($r < 4''$). A possible interpretation of this fact is that IR pumping has an important effect in the excitation of HCN $J = 1 - 0$. Also, the spatial resolution of the interferometric HCN $J = 1 - 0$ maps is poor to clearly identify any emitting region that could have importance in this fitting like high density regions. Thus, we ignored this transition for the density and temperature determination; we used only 3 – 2 and 13 – 12 transitions within the rotational diagram approach.

The value of E_{upp} of these two transitions are very different (12.8 and 387.0 K respectively) and so they probably trace different regions of the envelope as it can be seen in other species here presented. The properties derived for HCN would be a mix of these two different regions.

The opacities obtained for the two transitions are low (0.15 and 4.3×10^{-3} respectively) so no deviations are expected due to opacity effects. Mixing two regions is expected to derive higher temperatures for the external (cold) region as well as lower values of the density in the rotational diagrams. Thus, until further lines are observed to fill the gap between the two points presented in the HCN rotational diagram, the values of $T_{\text{rot}} = 51 \text{ K}$ and $N = 2.8 \times 10^{14} \text{ cm}^{-2}$ shall be regarded as intermediate values between that of the hot and the cold regions. If we use this column density and temperature to generate a synthetic HCN $J = 1 - 0$ profile, the result is significantly lower than the profile observed.

From the HCN 1 – 0 interferometric map we constrained the extent of this emission and the associated column density (Sect. 4.1). The line intensity observed in this interferometric map is compatible with that obtained with the IRAM 30m tele-

Table 6: Ratio between the abundance obtained for AFGL2233 (abundance in second column) and other sources ($X(\text{source})/X(\text{AFGL2343})$). *a*:Sánchez Contreras et al. (2014); *b*:(De Beck & Olofsson 2020); *c*:Quintana-Lacaci et al. (2016); *d*:Zhang et al. (2009); *e*:Bujarrabal et al. (1994); *f*:Agúndez et al. (2017). O-B94, C-B94 and S-B94 correspond to the average values for O-rich, C-rich and S-type stars respectively from Bujarrabal et al. (1994).

Molecule	AFGL2233	OH231 ^a	IK Tau ^b	IRC+10420 ^c	CIT 6 ^d	IRC+10216 ^b	WAql ^b	O-B94 ^e	C-B94 ^e	S-B94 ^e
CO	$3.6 \cdot 10^{-4}$	0.42	0.31	1.49	–	2.25	–	0.84	2.25	1.69
^{13}CO	$6.5 \cdot 10^{-6}$	7.72	2.16	11.6	–	–	–	1.70	3.71	–
HCN	$5.6 \cdot 10^{-7}$	0.04	1.18	1.96	2.14	17.9	5.54	0.66	13.2	7.14
H^{13}CN	$2.1 \cdot 10^{-7}$	–	0.39	0.67	0.96	–	–	–	–	–
HC_3N	$7.6 \cdot 10^{-7}$	0.01	–	–	1.71	0.26	1.11	0.30	2.90	–
H^{13}CCCN	$1.4 \cdot 10^{-8}$	–	–	–	–	–	–	–	–	–
HC_5N	$8.9 \cdot 10^{-8}$	–	–	–	145.5	0.90	–	–	–	–
SiO	$4.0 \cdot 10^{-7}$	0.10	20.1	3.27	1.76	0.15	0.73	24.7	1.79	40.3
^{29}SiO	$3.1 \cdot 10^{-8}$	–	58.8	9.14	2.58	–	–	–	–	–
^{30}SiO	$2.8 \cdot 10^{-8}$	–	47.1	9.78	2.90	–	–	–	–	–
SiS	$2.1 \cdot 10^{-7}$	0.14	22.2	0.34	16.4	0.96	7.24	3.47	10.6	–
CS	$2.1 \cdot 10^{-6}$	0.05	0.39	0.06	0.97	0.10	0.58	0.05	0.83	0.29
^{13}CS	$3.8 \cdot 10^{-8}$	–	2.24	–	4.00	–	–	–	–	–
C^{34}S	$1.3 \cdot 10^{-7}$	–	0.48	–	2.40	–	–	–	–	–
SiC_2	$7.6 \cdot 10^{-7}$	–	–	–	3.14	–	0.66	–	–	–
HNC	$1.4 \cdot 10^{-7}$	0.29	0.06	0.70	1.67	0.58	0.22	0.59	5.22	–
CCS	$6.7 \cdot 10^{-8}$	–	–	–	–	–	–	–	–	–
CCH	$1.1 \cdot 10^{-5}$	–	–	–	0.50	0.19	0.93	–	–	–
C_4H^a	$1.8 \cdot 10^{-7}$	–	–	–	22.4 ^f	–	–	–	–	–
C_4H^b	$2.0 \cdot 10^{-7}$	–	–	–	–	–	–	–	–	–
CN	$1.4 \cdot 10^{-5}$	–	0.01	0.10	1.92	0.07	0.42	–	–	–
CCCN	$1.7 \cdot 10^{-7}$	–	–	–	11.2	2.36	–	–	–	–

Table 7: Isotopic ratios derived comparing the derived molecular abundances.

Ratio	Value	From
$^{12}\text{C}/^{13}\text{C}$	55	CO
$^{12}\text{C}/^{13}\text{C}$	2.5–7.9	HCN
$^{12}\text{C}/^{13}\text{C}$	55	CS
$^{12}\text{C}/^{13}\text{C}$	57	HC_3N
$^{12}\text{C}/^{13}\text{C}$	7	C_3N
$^{32}\text{S}/^{34}\text{S}$	16	CS
$^{28}\text{Si}/^{29}\text{Si}$	13	SiO
$^{28}\text{Si}/^{30}\text{Si}$	14	SiO

scope. Also, it is worth noting that, even though the emission of this line is abnormally high, we can use this map to constrain the extent of the HCN emission. These values lead to an abundance value $> 1.1 \times 10^{-6}$. This value is low for C-rich AGBs but at the same time high if compared with that of standard O-rich AGBs (Bujarrabal et al. 1994, hereafter B94), but similar to that obtained for the yellow hypergiant star IRC+10420 (Quintana-Lacaci et al. 2016).

In order to understand the impact of the IR-pumping in the relative strength of the HCN $J = 1 - 0$ line, we imposed HCN $v > 0$ collisional rates to be 10^4 times lower than those of the known $v = 0$ values (Hernández Vera et al. 2017). With this approximation, and adopting the density and temperature values obtained from CO (see Table 2), we were able to fit the three observed transitions (see Fig. 5) by imposing a dust temperature of 900 K for $r < 5 \times 10^{15} \text{ cm}$ and 100 K beyond that radius until

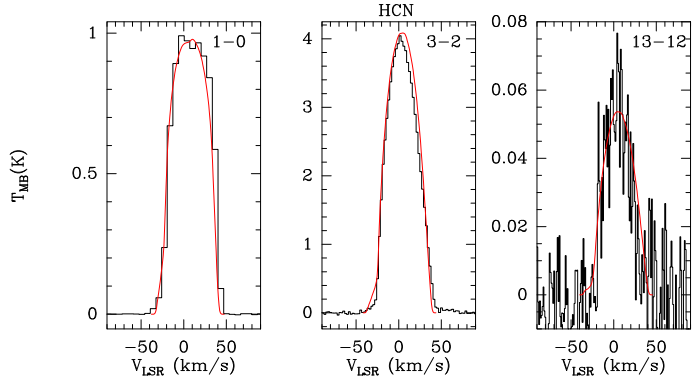


Fig. 5: Fitting of the HCN transitions observed, taking into account the IR-pumping.

7.8^{16}cm , which is the HCN $J = 1 - 0$ extent. This dust temperature distribution was meant to maximize the effect of the IR-pumping on the $J = 13 - 12$ transition in the innermost regions and that of the $J = 1 - 0$ in the outermost regions of the HCN emitting region, while keeping the balance for the $J = 3 - 2$ transition, which is affected by both regions. In order to fit the data we also had to scale the profiles, multiplying them by 0.92, 1.3 and 0.9 respectively. These values are within the calibration errors of the different telescopes and bands. The HCN abundance derived from this fitting is 10^{-5} , which is similar to those values obtained for C-rich AGB stars (Schöier et al. 2013).

The abundance derived for CN is $> 1.4 \times 10^{-5}$. This value is high for both C-rich and O-rich stars (except for CIT 6). On the contrary, HNC abundance ($\sim 1.4 \times 10^{-7}$) falls between both

chemical types, while HC_3N abundance is similar to that of C-rich AGB stars.

The adjustment of the rotational diagrams of H^{13}CN required two components. However, since we have observed that the IR-pumping plays an essential role in the excitation of the HCN lines, it might also impact on the H^{13}CN excitation (i.e. the LTE assumption is not valid in this case), specially on the $J = 1 - 0$ emission. Since, as it happens for HCN, we do not count with collisional rates for H^{13}CN , the derived LTE abundances are uncertain, and thus any isotopic ratio derived comparing both abundances would not represent the reality.

Six transitions of the different isomers H^{13}CCCN , HC^{13}CCN and HCC^{13}CN have been observed in total. However, due to sensitivity, only two lines were used to estimate the column density and rotational temperature.

4.3.3. C_3N & $^{13}\text{CCCN}$.

For AFGL 2233 the intensity of the C_3N lines is stronger than that of the C_4H lines, however for IRC +10216 (a well-studied nearby C-rich AGB star) the intensities of the C_3N lines are similar to those of the C_4H lines. Guelin et al. (1978) found that for IRC +10216 the abundance of C_4H is 4 times higher than that of C_3N . However, in our case the abundances are similar. If we compare case by case, in AFGL 2233 $X_{\text{C}_4\text{H}}$ is low compared with C-rich stars (IRC +10216 and CIT-6) and $X_{\text{C}_3\text{N}}$ is similar to that of IRC +10216 but low if compared with CIT 6.

To obtain the estimate of the column density of $^{13}\text{CCCN}$, since we only have detected a single line, we imposed the same temperature as for C_3N and, assumed LTE. The abundance obtained is $> 2.1 \times 10^{-8}$. The $^{12}\text{C}/^{13}\text{C}$ ratio derived for these species is ~ 8 , very low compared with the rest of the C-bearing molecules for which this ratio could be derived (see Table 7), except for HCN for which the derived value is uncertain (see Sect. 4.3.2). This suggests that the assumptions taken to derive the density of $^{13}\text{CCCN}$ might not be accurate.

4.3.4. Si-bearing species & CS

In general, the abundances derived for SiO and its isotopologues are low compared with O-rich stars as IK Tau or the values obtained by B94 for this type of objects (see Table 6). It is somehow similar to that of IRC+10420, however this object is known to have SiO constrained to a detached shell; this emission is suspected to arise from SiO freed from heated dust grains (Castro-Carrizo et al. 2001). On the other hand, these abundances are similar to those of CIT 6 and the values obtained for C-rich stars by B94.

The abundance derived for SiS is similar to that obtained by B94 for O-rich stars.

CS abundance is in general high compared with most of the estimates presented in Table 6, but closer to that of C-rich stars. The opacities derived from the two transitions observed are 0.27 and 0.40 for $J = 2 - 1$ & $J = 5 - 4$ respectively. Interestingly, the ^{13}CS abundance is similar (~ 2 and ~ 4 times lower) in AFGL 2233 compared with IK Tau and CIT 6 respectively. This shows a clear difference in the carbon isotopic ratio between these objects. In the case of AFGL 2233, regarding CS, $^{12}\text{C}/^{13}\text{C}$ is 55, while for IK Tau is 9.5 and 13.3 for CIT 6. These values have evolutionary implications as shown by Milam et al. (2009) (see below for a further discussion on the isotopic ratios).

We compared the abundances obtained for these species for AFGL 2233 with those derived for a large number of C-rich

and O-rich AGB stars by Massalkhi et al. (2019) and Massalkhi et al. (2020) respectively (see Fig. 6). The SiO and SiS abundances of AFGL 2233 do not clearly suggest an O-rich or C-rich behaviour. Only for CS AFGL 2233 falls clearly within the C-rich region. Even though it might seem that CS abundance of AFGL 2233 follows the $X_{\text{CS}}(V_{\text{exp}})$ trend of the O-rich AGBs, the values obtained for massive evolved stars are not higher than several times 10^{-7} (Quintana-Lacaci et al. 2007, 2016; Ziurys & Richards 2025), well below the values found for C-rich stars (and AFGL 2233).

4.3.5. C_2H & C_4H

These two species are only detected in sources presenting a C-rich chemistry in their circumstellar envelopes. However, the abundances here obtained for C_2H and C_4H are respectively higher and lower than in typically found in C-rich stars (such as CIT 6 and IRC +10216).

Despite the number of lines observed for C_2H (16), their E_{up} are 4.2 K or ~ 25 K for all of them. Therefore, the values obtained via de rotational diagrams might be not accurate. We confirmed the values obtained modeling the observed lines using MADEX, in the LTE approach. The results so obtained are $N = 3.6 \times 10^{15} \text{ cm}^{-2}$ and $T_{\text{rot}} = 12$ K (see fitting in Fig. 7). These results are very similar to those presented in Table 5. The C_2H abundance is also very similar to the value derived by Fuente et al. (1998).

The formation of both species, C_2H and C_4H , is deeply connected. The formation paths are (see Agúndez et al. 2017):



Agúndez et al. (2017) found that, for IRC +10216, the regions where the emission from these species arise are similar. Thus, the processes taking place (i.e. photodissociation, eqs. 1 and 3), should have similar impact for both molecules. However, as C_4H is relatively underabundant in our case, there should be a process – or contrary a process is not taking place –, which as result avoids or limits the formation of C_4H compared with C_2H .

Fuente et al. (1998) showed that C-rich AGBs with high expansion velocities, i.e. the HVC stars, present high C_2H abundances when compared with standard low-velocity C-rich AGB stars. These authors suggested that the higher expansion velocity could prevent acetylene to stick to grains, compared to objects with low expansion velocities (as the depletion radius is proportional to $V_{\text{exp}}^{3/2}$). This would result in more acetylene available to be photodissociated into C_2H via reaction (1). However, this would also affect C_4H in the same manner (reactions (2) & (3)), contrary to what is observed.

Other option would be that the formation of C_2H is enhanced. In particular, there is another path to form this latter species, related to the abundance of HC_3N .



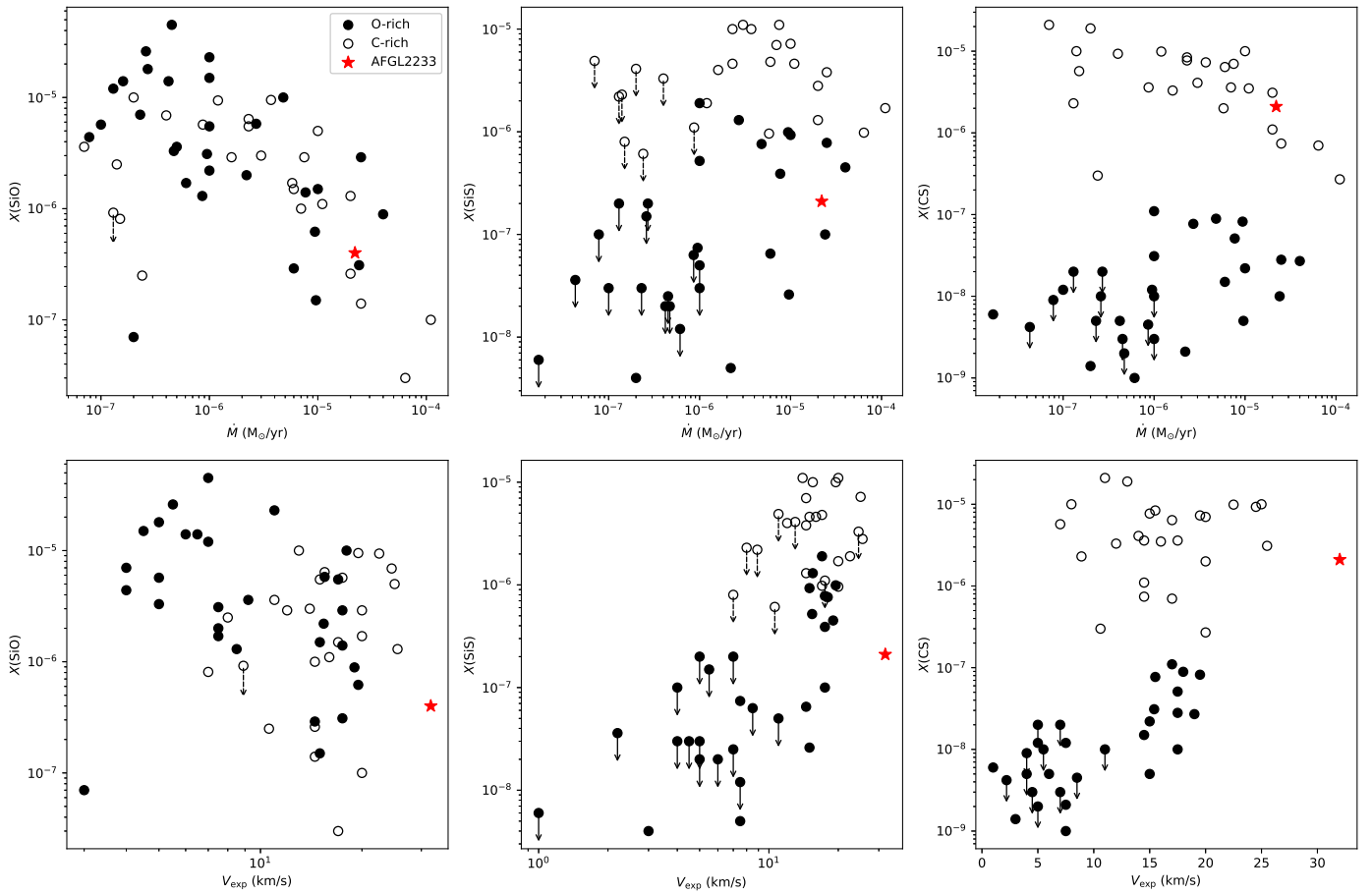


Fig. 6: Comparison of the SiO, SiC and CS abundances obtained for C-rich AGB stars (Massalkhi et al. 2019) and O-rich AGBs (Massalkhi et al. 2020) with those obtained for AFGL 2233, with respect to the mass-loss rates and the expansion velocities.

In order to try to understand the differences observed, we ran chemical models as those presented by Agúndez et al. (2017), varying both of the inputs for the reactions cited, i.e. acetylene and HCN. The characteristics of the circumstellar gas used for the chemical model is an average of the two inner shells fitted in Sect. 3.2. The results are presented in Fig. 8.

It can be seen that the impact of enhancing the HCN abundance has only a minor effect on the C_2H/C_4H abundance ratio, with a decrease of both species of $\sim 15\%$, being this small difference the responsible for the (small) increase in the ratio observed in the figure. On the contrary, note that varying the abundance of HCN has, however, a clear impact on the HC_3N abundance, which does not seem to severely affect the formation of C_2H via reaction (6).

However, if we modify the amount of acetylene available, the C_2H/C_4H abundance ratio presents significant changes. In particular, the abundance ratio here derived is ~ 58 , while for CIT 6 or IRC +10216 is close to 1. As observed in Fig. 8, the large ratios observed in AFGL 2233 could be reached in cases of low acetylene abundances.

This increase in the ratio is due to that the reactions (1) to (4) are essential to the formation of C_4H ; but while it also affects the formation of C_2H , this molecule could be formed via reaction (6), i.e. with no acetylene involved. Thus low abundance of acetylene would minimize reactions (1) to (4), severely affecting the abundance of C_4H , while C_2H could still be formed.

Despite this, ISO observations, as those presented by Yang et al. (2004) showed that this object clearly shows a strong presence of acetylene, as predicted by (Fuente et al. 1998).

Interestingly, this ratio has been found to be high in PDRs compared with AGB stars (see e.g. Teyssier et al. 2004). Our chemical models showed the same trend. We modeled the column densities resulting after increasing the standard interstellar radiation field (Draine 1978) by a factor 1, 3, 10 and 100 and found that the ratio C_2H/C_4H increases from ~ 9 to ~ 17 (Fig. 9). This suggests that photochemistry might be the source of this high ratio. We note that the models used to check the variations of the $X(C_2H)/X(C_4H)$ ratio assumed an average value of the gas properties obtained in Table 2 for the regions where C_2H is observed, since we are interested in checking ratio trends qualitatively, rather than obtaining quantitative estimates of the UV field, for what we of lack essential information.

4.3.6. NH_3

Ammonia has been also detected toward this object with HIFI (see Table A.1). In particular, the transition $1_{0,0} - 0_{0,1}$ of ortho- NH_3 was observed with HIFI. This is the only line observed of this species in AFGL 2233.

Since we count with density and temperature profiles, and collisional rates for this molecule, we modeled the line emission using the LVG approach with MADEX.

As the regions and the mechanisms responsible for the NH_3 formation are not clear (see e.g. Agúndez et al. 2020), we as-

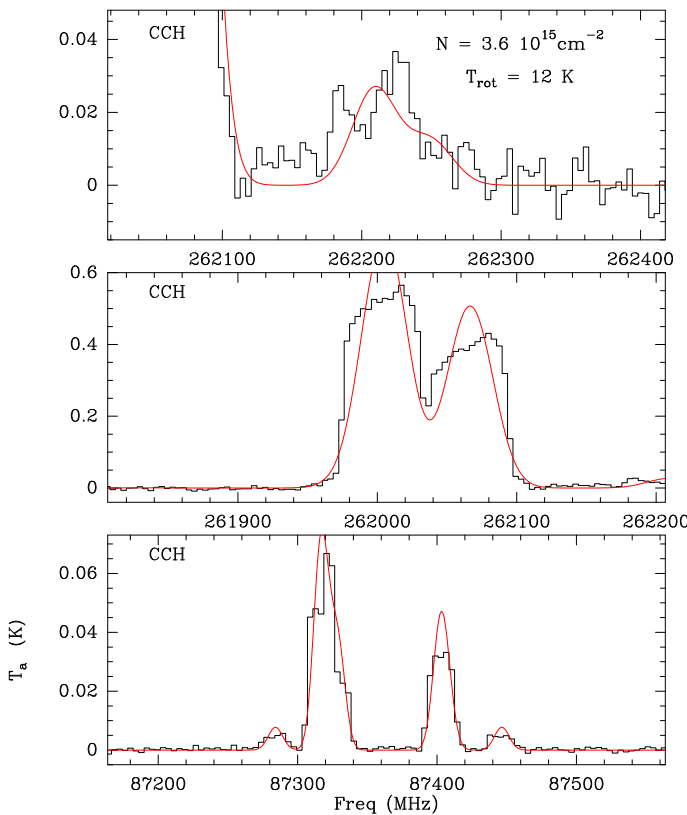


Fig. 7: LTE fitting of the CCH line emission.

sumed a similar distribution as found for IRC +10216 (Schmidt et al. 2016), scaled for the mass loss properties derived for this object, i.e. $R_{\text{out}} \sim 5 \times 10^{16} \text{ cm}$, and used the temperature and density profiles obtained above (see Table 2).

The abundance value obtained, X_{NH_3} of 2.5×10^{-5} , is high compared with those derived for other objects. The only source with a similar abundance is W Aql (1.7×10^{-5} , De Beck & Olofsson 2020). In case the emitting region is smaller the abundance needed to fit the profile must be higher. However, if we assume the extent of NH_3 is similar to that derived to CO, the abundance needed is similar, but in addition the synthetic profile obtained presents clear self-absorption. Therefore, the values of the abundance and outer radius reported above seem to be accurate. The result of the fitting can be seen in Fig. 10.

Menten et al. (2010) studied the abundances of ammonia in different objects O-rich objects. They found that the abundance of ammonia was high ($2 \times 10^{-7} - 3 \times 10^{-6}$). On the contrary, the value obtained for IRC +10216 (Schmidt et al. 2016) was significantly lower (4×10^{-8}). The value obtained here is the higher reported for an evolved star. However, it must be kept in mind that, as in the work by Menten et al. (2010), our model does not take into account the effect of the IR pumping, and thus could lead to an overestimate of the ammonia abundance. Wong et al. (2018) confirmed this fact, showing that the abundance estimate was few times lower. In any case, regardless of this possible modeling issue, since the correction factors obtained by Wong et al. (2018) are rarely an order of magnitude, the abundance of ammonia in this object, while not being accurate, would still be extremely high.

While the higher abundance observed in O-rich (high-mass) stars could be associated with an enhanced abundance of Nitrogen as expected for the Hot Bottom Burning (HBB) process taking place in these objects, Wong et al. (2018) found it to arise

Table 8: Intensity of the water transitions observed in T_a^* (K), Jy, and corrected by distance, I_d .

H_2O trans.	I (Jy)	T_a^* (mk)	I_d ($\text{K km s}^{-1} \text{ pc}^2$)
$1_{1,0} - 1_{0,1}$	1.2	36.8	2.0×10^6
$1_{1,1} - 0_{0,0}$	4.9	55.7	2.9×10^6

from clumpy structures. These authors suggested NH_3 emission traces swept-up material, suggesting that shocks might also contribute to the formation of ammonia.

4.3.7. H_2O

Two molecular lines of H_2O have been detected in the envelope of AFGL 2233. If we compare the intensity of these transitions with those observed in IRC +10216 (Neufeld et al. 2011), the prototypical C-rich AGB stars, and in O-rich objects (Justtanont et al. 2012), we find that those of the HVC stars are more intense than expected.

In particular, for IRC +10216, the intensity obtained for the $11_{1,0} - 10_{0,1}$ transition is lower than 0.5 K (in T_a^*) and ~ 0.6 K for $11_{1,1} - 0_{0,0}$ (Neufeld et al. 2011). If we scale the fluxes found for AFGL 2233 (table A.1) with the distance of IRC +10216 (130pc, Agúndez et al. 2012) these fluxes would be 3.5 and 5.3 K respectively, $\sim 7-9$ times higher than those of IRC +10216. Note that the mass loss rates are similar for both objects Velilla-Prieto et al. (2019).

If we compare the integrated intensities of these lines (see Table 8) with the distance-corrected integrated intensities presented by Justtanont et al. (2012) we find that those reported here are higher than those of W Hya, R Dor, o Cet, R Cas, IK Tau and TX Cam, slightly lower than that of IRC +10011, AFGL 5379 and OH 26.5+0.6. Also, it is interesting to remark that the relation between the mass loss ($1.8 \times 10^{-5} M_{\odot} \text{ yr}^{-1}$ for the innermost shell where H_2O is expected to be located), and the intensity of the water lines follows the same trend as that observed in O-rich stars (Fig 2, Justtanont et al. 2012).

In the case of C-rich evolved stars, it has been shown that H_2O is located in the inner regions of the envelopes, either if its formation is related with shocks (Cherchneff 2011), photochemistry due to clumpiness (Agúndez et al. 2010), being the latter the most extended H_2O formation radius ($40-400 \text{ au} \sim 6 \times 10^{14} - 6 \times 10^{15} \text{ cm}$).

To obtain an estimate of the water abundance we run a LVG code (colisional rates from Daniel et al. 2011), adopting the density and temperature profiles obtained for CO (table 2), and an ortho/para ratio of 3 (Neufeld et al. 2011). We tried to model the emission adopting an outer radius for H_2O as that suggested by Saavik Ford & Neufeld (2001), but we could not fit both line intensities simultaneously. The best fit was obtained restricting the emission to the innermost shell presented in Table 2 ($R_{\text{out}} = 5 \times 10^{16} \text{ cm}$). Even though this extent is large for what has been found for the H_2O emission in evolved stars, the abundance obtained for H_2O was very high for a C-rich object and similar to what would be expected for an O-rich evolved star (see e.g. Agúndez et al. 2010): 7.5×10^{-5} and 2.5×10^{-5} for o- H_2O and p- H_2O respectively. It is worth noting that this value is directly related to the mass located within the shell assumed to be the origin of such emission; if the emitting region is more compact, this abundance will be even higher.

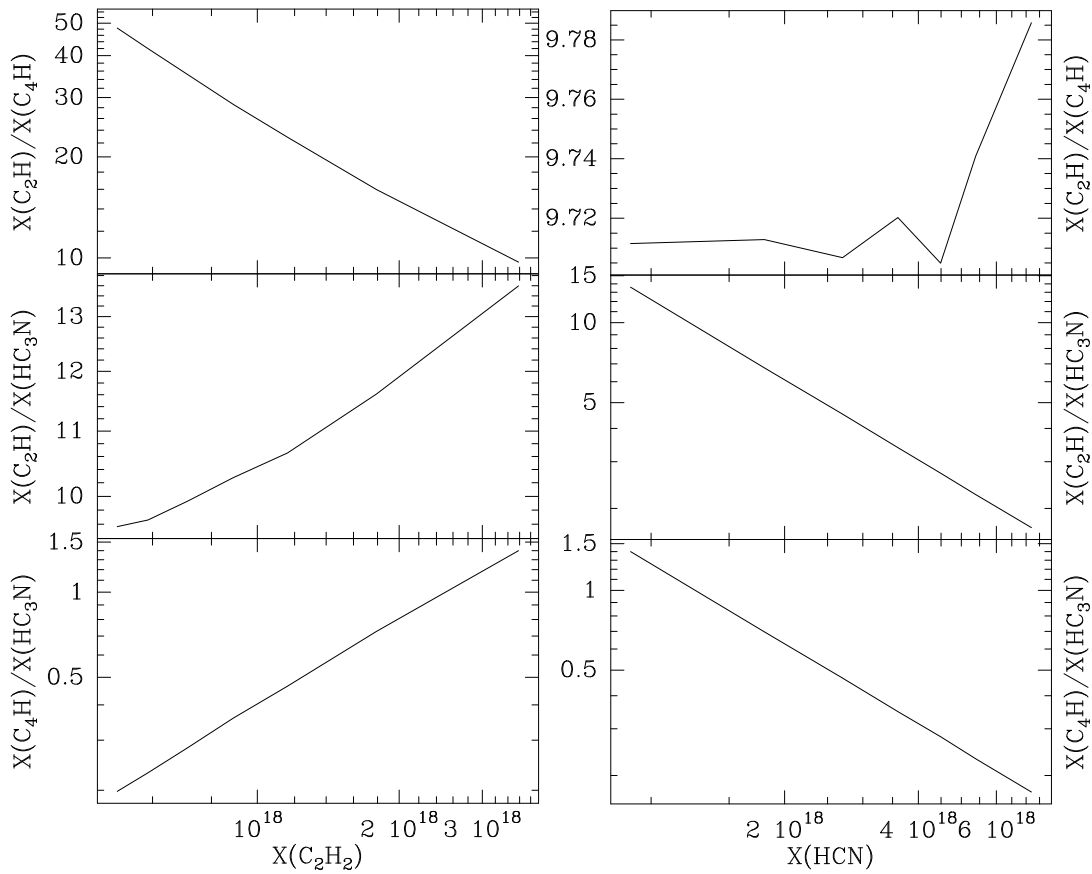


Fig. 8: Variations of the abundance ratios $X(C_2H)/X(C_4H)$ (top), $X(C_2H)/X(HC_3N)$ (middle) and $X(C_4H)/X(HC_3N)$ (bottom). Left: HCN abundance is kept constant while varying that of C_2H_2 . Right: C_2H_2 abundance is kept constant while varying that of HCN.

4.3.8. SiN

SiN is a peculiar species. It has been found only in very few objects: W Aql (De Beck & Olofsson 2020) – a S-type star –, IRC +10216 (Turner 1992) – C-rich star –, and η Car (Bordiu et al. 2022) – a massive evolved star. This would be the fourth detection of this species in the circumstellar gas.

The origin of the formation of this species has been discussed and linked both to the triggering of chemical reactions by a binary (Danilovich et al. 2024) or to the presence of a Nitrogen-enriched medium (Bordiu et al. 2022).

Since the two transitions observed are too close in energy, the rotational diagram methodology is not a good approach to determine the abundance of SiN . Similarly to what we have done for ammonia and water, we used the temperature and density profiles obtained from CO observations, and model the data using an LTE approach (there are not SiN collisional rates available), assuming the most probable location of SiN .

It is worth noting that NH_3 has been found to be particularly abundant in this object. The abundance of ammonia might have a direct impact in the detection of SiN , since, as proposed by (Danilovich et al. 2024), the main path for the formation of SiN is:



Also, the main source of formation of Si^+ is the photodissociation of SiS . As a first approach we assume the same extent of

SiO and SiS (7×10^{16} cm, see table 3), which, as shown by Masalkhi et al. (2024) is reasonable for objects with $\dot{M}/v_{exp} > 10^{-6} M_\odot \text{ yr}^{-1} \text{ km}^{-1} \text{ s}$ (for AFGL 2233 this value ranges from 7×10^{-7} to $1.2 \times 10^{-6} M_\odot \text{ yr}^{-1} \text{ km}^{-1} \text{ s}$). As we expect Si^+ to appear further than shell 1 (table 2) we ignored this shell in the fitting.

Furthermore, we note that when assuming that the extent of SiN as arising from shells 2–4, the profiles presented a horned-like shape, suggesting that the extent assumed was larger than that observed – the line profiles do not present that horned shape. Therefore, we constrained the extent to just shell 2.

The result of the fitting is presented in Fig. 12. To check the validity of our model fitting the two well-detected lines, we also obtained synthetic spectra for all the SiN transitions covered by our survey. As shown in the figure, the fitting also predicts the non-detections of the rest of the transitions – tentative detection in the case of SiN 6–5(11/2–9/2) (at 261650.18 MHz).

The abundance derived is $X_{SiN} = 7 \times 10^{-8}$. This abundance is 2 times lower than that observed in W Aql (Danilovich et al. 2024), and 2 times larger than that of η Car (Bordiu et al. 2022). It is worth noting that SiN has not been detected in other massive objects such as IRC +10420 (Quintana-Lacaci et al. 2016), VY CMA or AFGL 2343 (priv. comm.), objects that, as observed in IRC +10420 (Quintana-Lacaci et al. 2013), are expected to present a N-rich enrichment.

5. Discussion

We have obtained the fractional abundances of different species toward the HVC star AFGL 2233. At first sight, its chemistry

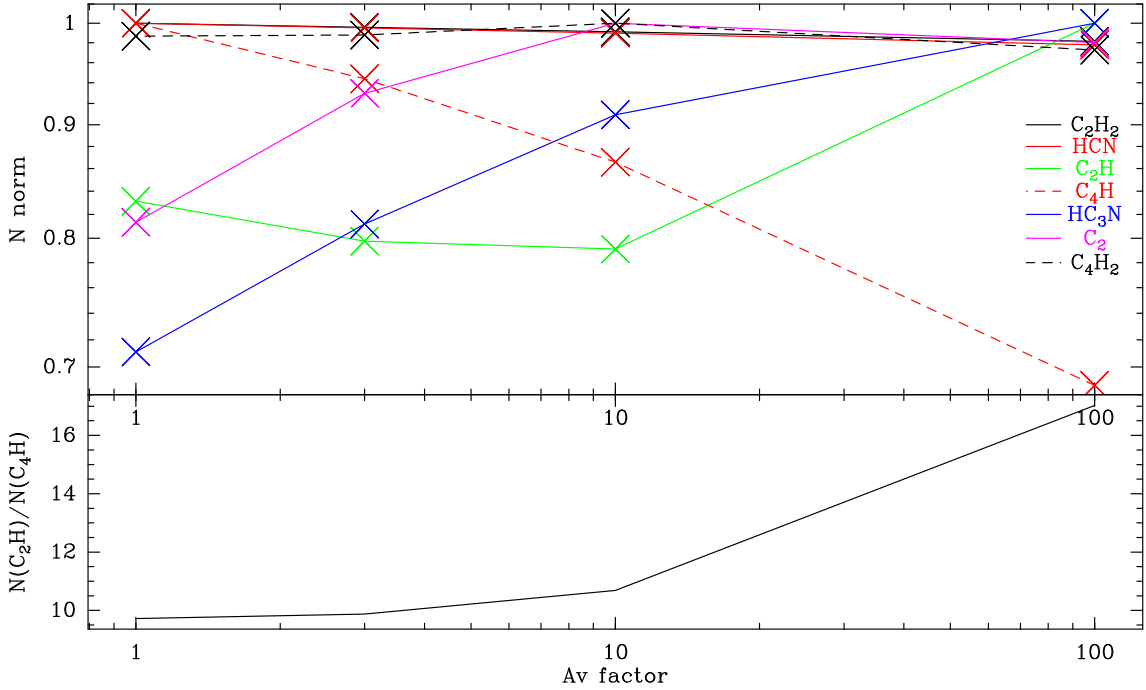


Fig. 9: Chemical model result of the column densities (normalized for comparison purposes) for different values of radiation field (top). Variation of the column density ratio C_2H/C_4H for different values of radiation field (bottom).

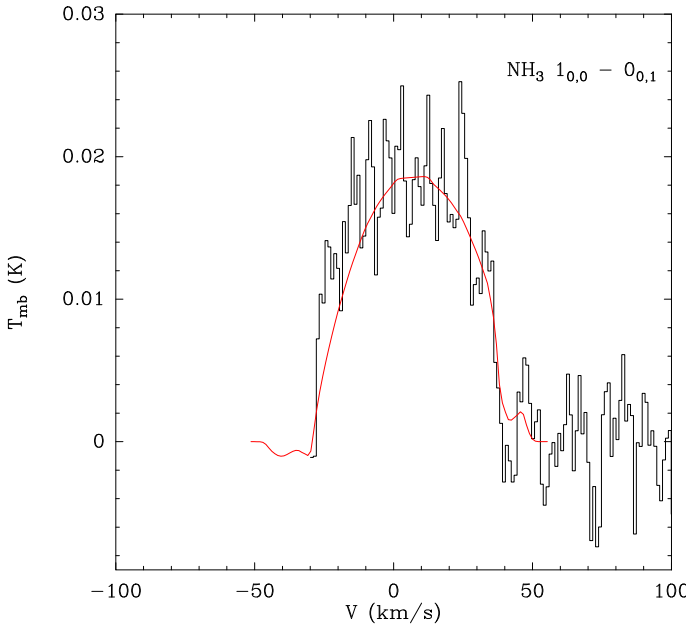


Fig. 10: Fitting of the NH_3 $1_{0,0} - 0_{0,1}$ line.

and the abundances obtained are in general compatible with a standard C-rich star rather than with a massive star in its O-to-C chemical transition – after the exhaustion of the HBB. However certain results reveal the peculiar nature of this object.

While we found no strong signs of ^{14}N enrichment compared with other objects, as the yellow hypergiant star IRC +10420, and the abundances of N-bearing species are compatible with a C-rich chemistry, certain facts might support the presence of a N-rich medium: the C_2H/C_4H ratio suggest a lack of acetylene in the circumstellar gas, compared with HC_3N , and the very high abundance of NH_3 . Also SiN has been detected in this object,

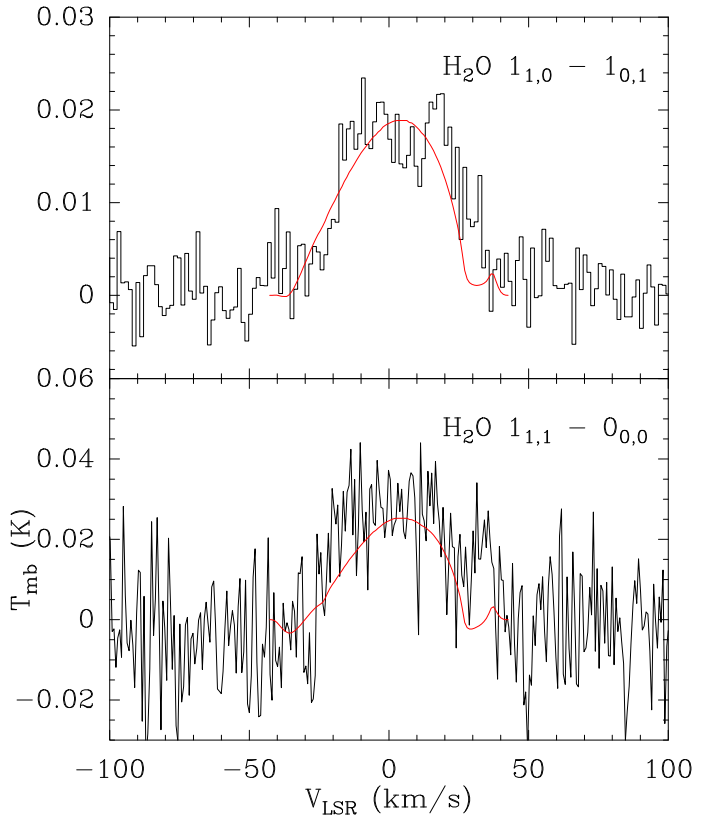


Fig. 11: Fitting of the H_2O $1_{1,0} - 1_{0,1}$ and $1_{1,1} - 0_{0,0}$ lines.

which has been related with the presence of N-enrichment in massive stars (Bordiu et al. 2022).

The values obtained for $^{12}C/^{13}C$ – those for which the abundances derived were trustworthy – were 55–57. These values are associated with CO, CS and HC_3N . Opacity effects have been

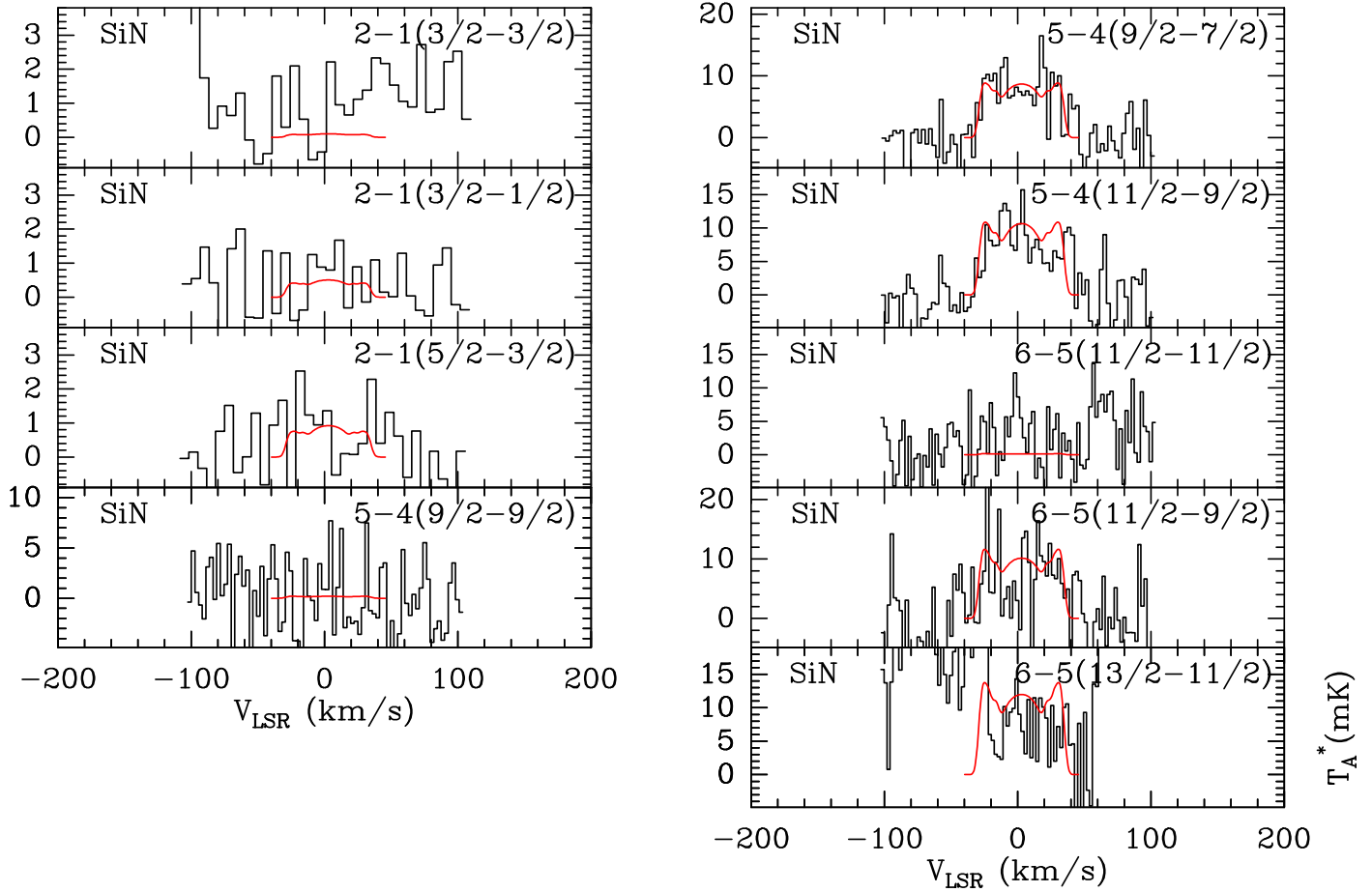


Fig. 12: Fitting of the SiN transitions covered by the line survey.

discarded, and the quality of the fits was reliable. In the case of C_3N , the isotopic ratio relies on the assumption of similar rotational temperatures for both isotopologues, however these species are expected to arise from very similar regions, an extended and narrow shell (Agúndez et al. 2017). Therefore the low value of ~ 8 probably accurate, at least at that region.

Milam et al. (2009) and Ramstedt & Olofsson (2014) show that low $^{12}\text{C}/^{13}\text{C}$ ratios are typical of O-rich circumstellar envelopes, whereas higher ratios are generally associated with C-rich evolved stars. In addition, a high water abundance has been derived, comparable to that found in O-rich objects. These results are difficult to reconcile within a consistent evolutionary scenario.

We can divide these results into two categories according to the regions traced by the different species: 1) results obtained for gas extending from the innermost regions to the outer regions (CO, SiO, and in some extent HC_3N), and 2) results constrained to a thin shell structure ($\text{C}_2\text{H}/\text{C}_4\text{H}$, C_3N). Note that while the assumed ring-like structure assumed for HC_3N and C_2H is the same, interferometric maps of IRC +10216 (Agúndez et al. 2017) showed that the former species presents a smaller central hole, with a more smooth slope, while C_2H and C_3N present narrower and steeper slopes. In addition, as the same assumption is applied to all isotopologues, the abundance ratio does not depend on those assumptions.

The results obtained for the species extending along the CSE could trace a mixture of photospheric initial abundances – for example, photospheric abundances evolving with time, creating a gradient in the CSE abundance ratios –, being those of a C-rich

media the ones dominating the results obtained. On the contrary, the results arising from the constrained region traced by a narrow outer ring does not suffer from this mixing.

In any case, the "ring-constrained" species (C_3N , C_2H , C_4H ,...) have not been detected in O-rich evolved stars. This region presents a C-rich chemistry ($\text{C}/\text{O} > 1$) but with low $^{12}\text{C}/^{13}\text{C}$, which is characteristic of objects evolving from an O-rich regime to a C-rich regime after the exhaustion of the HBB (e.g. Karakas et al. 2018). The further evolution of those objects would lead to C-rich envelopes with carbon isotopic ratios as those traced by CS or CO.

We might wonder if the evolution is from a C-rich (extended) environment evolving towards a O-rich medium after the activation of the HBB, but models do not predict such scenario. However, these mixed characteristics have been previously observed in pre-planetary nebulae (pPNe) objects (García-Hernández et al. 2016). These authors observed OH and H_2O in C-rich pPNe with high mass losses. These results are interpreted as a result of a CO photodissociation, leading to a transitory O-rich chemistry as predicted by Cernicharo (2004).

This O-rich chemistry – in particular the presence of H_2O –, the high abundance of NH_3 and the presence of SiN, which has been also related to a photoinduced chemistry due to the presence of a hot binary (Danilovich et al. 2024), might suggest that the anomalies found are related to the presence of a similar binary system rather to a nucleosynthesys-related C-to-O change. Also, the presence of a hot binary-induced photochemistry could explain the high $\text{C}_2\text{H}/\text{C}_4\text{H}$ abundance ratio derived.

The effect of the IR-pumping has been found to be very important in the case of HCN, and, as suggested, it might also be important in the case of –at least– NH₃. The abundance of this latter molecule has to be regarded as an upper limit.

Further high-angular resolution observations of the different isotopologues might allow to study the gradient of ¹²C/¹³C along the radius of the CSE, i.e. how this ratio has evolved during the recent evolution of the star. Also, probing the regions emitting SiN, and C₂H and C₄H could confirm the presence of the photoinduced chemistry and the possible presence of a companion.

The impact of a companion, in addition to the chemical signatures, could also appear in the width of the profiles. It has been shown that the expansion velocity of the gas in the orbital plane could be significantly enhanced (Bermúdez-Bustamante et al. 2020). It could be the case that the large line width observed in AFGL 2233 is due to that the orbital plane is close to edge-on w.r.t. to us. However, the luminosity, even for the revisited distance is still too high for a C-rich intermediate-mass AGB star, suggesting initial masses in the range 4 – 9M_⊙ (see Sect. 3.1).

This object might represent a mixture of both scenarios: a C-rich massive evolved stars resulting from exhausted HBB, combined with a binary companion triggering localized photoinduced chemistry. High angular-resolution interferometric molecular line maps could confirm this scenario, or suggest a new one.

It is worth noting that, as stated by Javadi et al. (2011), RSG stars cannot undergo a HBB process, thus, these objects would no undergo a O-to-C transition in their photospheres and subsequently in their ejecta. Only massive AGBs and super-AGBs would present this process. More massive stars, such as RSGs or yellow hypergiants – which do not present TDU or HBB – presenting N-enrichment are probable a result of intense mass loss events exposing inner layers rich in CNO processed elements or other processes such as e.g. convection or rotation-induced mixing (Schootemeijer et al. 2019). Thus, since only AGB stars present HBB – and therefore its exhaustion – AFGL 2233 should probably be a massive (super-)AGB rather than a RSG.

6. Conclusions

We first re-estimated the luminosity and temperature and density profiles for AFGL 2233 according to the new Gaia DR3 distance. Even though the new distance sets this source significantly closer, its luminosity still suggests that AFGL 2233 is a massive AGB star, with $M_{\text{init}} = 4.5\text{--}9M_{\odot}$. This would explain the origin of the wide molecular-line profiles observed.

We studied the chemistry of the HVC star AFGL 2233. We aimed at finding hints of the massive nature of this object. However, we found a standard C-rich chemistry except for certain peculiar features, which are:

- High C₂H/C₄H abundance ratio (probably related to photoinduced chemistry).
- Very high NH₃ abundance (the highest observed so far – IR-pumping can lower this value).
- High H₂O abundance (comparable with O-rich stars).
- SiN detected (fourth time detected in an evolved star).

The isotopic ratios present larger changes (from 55 to 7) but currently it is hard to clearly determine if, as expected if this object is being enriched in ¹²C after the HBB has been exhausted, i.e. a higher ¹²C/¹³C in the inner regions than in the outer shells. Dedicated high-angular resolution observations are needed to confirm if this is the case.

In addition, the mentioned peculiarities seem to point toward the possible presence of a companion, triggering both the formation of SiN, and H₂O, while also increasing the C₂H/C₄H abundance ratio. Carefully tracing the regions where these species arise could help to confirm the presence of that companion and constrain the region where the suggested binary-induced photochemistry might take place.

Acknowledgements. The research leading to these results has received funding funding support from Spanish Ministerio de Ciencia, Innovación, y Universidades through grant PID2023-147545NB-I00. JA is partially supported by I+D+i projects 1010 PID2019-105203GB-C21 and PID2023-146056NB-C21, funded by the Spanish MCIN/AEI/10.13039/501100011033 and EU/ERDF. LVP contribution is supported by project PID2020-117034RJ-I00. This publication is part of the grant RYC2023-045648-I funded by MICI/AEI/10.13039/501100011033 and by ESF+. This work has made use of data from the European Space Agency (ESA) mission *Gaia* (<https://www.cosmos.esa.int/gaia>), processed by the *Gaia* Data Processing and Analysis Consortium (DPAC, <https://www.cosmos.esa.int/web/gaia/dpac/consortium>). Funding for the DPAC has been provided by national institutions, in particular the institutions participating in the *Gaia* Multilateral Agreement.

References

Agúndez, M., Cernicharo, J., & Guélin, M. 2010, ApJ, 724, L133
 Agúndez, M., Cernicharo, J., Quintana-Lacaci, G., et al. 2017, A&A, 601, A4
 Agúndez, M., Fonfría, J. P., Cernicharo, J., et al. 2012, A&A, 543, A48
 Agúndez, M., Martínez, J. I., de Andres, P. L., Cernicharo, J., & Martín-Gago, J. A. 2020, A&A, 637, A59
 Alcolea, J., Bujarrabal, V., Planesas, P., et al. 2013, A&A, 559, A93
 Andrae, R., Fouesneau, M., Sordo, R., et al. 2023, A&A, 674, A27
 Bermúdez-Bustamante, L. C., García-Segura, G., Steffen, W., & Sabin, L. 2020, MNRAS, 493, 2606
 Bordiu, C., Rizzo, J. R., Bufano, F., et al. 2022, ApJ, 939, L30
 Bujarrabal, V., Fuente, A., & Omont, A. 1994, A&A, 285, 247
 Castro-Carrizo, A., Lucas, R., Bujarrabal, V., Colomer, F., & Alcolea, J. 2001, A&A, 368, L34
 Cernicharo, J. 1985, IRAM internal report No. 52
 Cernicharo, J. 2004, ApJ, 608, L41
 Cernicharo, J. 2012, in ECLA-2011: Proceedings of the European Conference on Laboratory Astrophysics, European Astronomical Society Publications Series
 Cherchneff, I. 2011, A&A, 526, L11
 Daniel, F., Dubernet, M.-L., & Grosjean, A. 2011, A&A, 536, A76
 Danilovich, T., Malfait, J., Van de Sande, M., et al. 2024, Nature Astronomy, 8, 308
 De Beck, E. & Olofsson, H. 2020, A&A, 642, A20
 de Graauw, T., Helmich, F. P., Phillips, T. G., et al. 2010, A&A, 518, L6
 Draine, B. T. 1978, ApJS, 36, 595
 Fuente, A., Cernicharo, J., & Omont, A. 1998, A&A, 330, 232
 Gaia Collaboration, Prusti, T., de Bruijne, J. H. J., et al. 2016, A&A, 595, A1
 Gaia Collaboration, Vallenari, A., Brown, A. G. A., et al. 2023, A&A, 674, A1
 García-Hernández, D. A., García-Lario, P., Cernicharo, J., Engels, D., & Pereira-Calderón, J. V. 2016, in Journal of Physics Conference Series, Vol. 728, Journal of Physics Conference Series (IOP), 052003
 Girardi, L., Bressan, A., Bertelli, G., & Chiosi, C. 2000, A&AS, 141, 371
 Goldsmith, P. F. & Langer, W. D. 1999, ApJ, 517, 209
 Guelin, M., Green, S., & Thaddeus, P. 1978, ApJ, 224, L27
 Habing, H. J. & Olofsson, H., eds. 2003, Asymptotic giant branch stars
 Hernández Vera, M., Lique, F., Dumouchel, F., Hily-Blant, P., & Faure, A. 2017, MNRAS, 468, 1084
 Javadi, A., van Loon, J. T., & Mirtorabi, M. T. 2011, MNRAS, 414, 3394
 Justtanont, K., Khouri, T., Maercker, M., et al. 2012, A&A, 537, A144
 Karakas, A. I., Lugaro, M., Carlos, M., et al. 2018, MNRAS, 477, 421
 Likkel, L. & Miao, Y. 1996, AJ, 112, 301
 Loup, C., Forveille, T., Omont, A., & Paul, J. F. 1993, A&AS, 99, 291
 Massalkhi, S., Agúndez, M., & Cernicharo, J. 2019, A&A, 628, A62
 Massalkhi, S., Agúndez, M., Cernicharo, J., & Velilla-Prieto, L. 2020, A&A, 641, A57
 Massalkhi, S., Agúndez, M., Fonfría, J. P., et al. 2024, A&A, 688, A16
 Menten, K. M., Wyrowski, F., Alcolea, J., et al. 2010, A&A, 521, L7
 Meynet, G. & Maeder, A. 2003, A&A, 404, 975
 Milam, S. N., Woolf, N. J., & Ziurys, L. M. 2009, ApJ, 690, 837
 Neufeld, D. A., González-Alfonso, E., Melnick, G. J., et al. 2011, ApJ, 727, L28
 Pardo, J. R., Cernicharo, J., & Serabyn, E. 2001, IEEE Trans. on Antennas and Propagation, 49/12, 1683
 Pilbratt, G. L., Riedinger, J. R., Passvogel, T., et al. 2010, A&A, 518, L1

Quintana-Lacaci, G., Agúndez, M., Cernicharo, J., et al. 2013, A&A, 560, L2

Quintana-Lacaci, G., Agúndez, M., Cernicharo, J., et al. 2016, A&A, 592, A51

Quintana-Lacaci, G., Bujarrabal, V., Castro-Carrizo, A., & Alcolea, J. 2007, A&A, 471, 551

Quintana-Lacaci, G., Cernicharo, J., Agúndez, M., et al. 2019, The Astrophysical Journal, 876, 116

Ramstedt, S. & Olofsson, H. 2014, A&A, 566, A145

Roelfsema, P. R., Helmich, F. P., Teyssier, D., et al. 2012, A&A, 537, A17

Saavik Ford, K. E. & Neufeld, D. A. 2001, ApJ, 557, L113

Sánchez Contreras, C., Velilla, L., Alcolea, J., et al. 2014, in Asymmetrical Planetary Nebulae VI Conference, ed. C. Morisset, G. Delgado-Inglada, & S. Torres-Peimbert, 88

Schmidt, M. R., He, J. H., Szczerba, R., et al. 2016, A&A, 592, A131

Schöier, F. L., Ramstedt, S., Olofsson, H., et al. 2013, A&A, 550, A78

Schootemeijer, A., Langer, N., Grin, N. J., & Wang, C. 2019, A&A, 625, A132

Teyssier, D., Fossé, D., Gerin, M., et al. 2004, A&A, 417, 135

Turner, B. E. 1992, ApJ, 388, L35

Velilla-Prieto, L., Cernicharo, J., Agúndez, M., et al. 2019, A&A, 629, A146

Wong, K. T., Menten, K. M., Kamiński, T., et al. 2018, A&A, 612, A48

Yang, X., Chen, P., & He, J. 2004, A&A, 414, 1049

Yuasa, M., Unno, W., & Magono, S. 1999, PASJ, 51, 197

Zhang, Y., Kwok, S., & Dinh-V-Trung. 2009, ApJ, 691, 1660

Ziurys, L. M. & Richards, A. M. S. 2025, Galaxies, 13, 82

Appendix A: Line properties

Below we list the main properties of the lines observed with IRAM 30m and HIFI.

Table A.1: Line transitions detected toward AFGL 2233.

ν_{rest} (MHz)	Molecule	Transition	T _A * (mK)	Area (K km/s)	Notes
71889.595	HC ₅ N	27–26	10.00 ± 2.8	0.65	T _A *
72475.060	HC ¹³ CCN	8–7	5.00 ± 2.3	0.38	T _A *
72618.112	SiS	4–3	5.00 ± 2.4	0.41	T _A *
72783.818	HC ₃ N	8–7	80.00 ± 2.6	4.73	T _A *
74551.987	HC ₅ N	28–27	7.00 ± 2.0	0.56	T _A *
76117.477	C ₄ H	8–7	3.00 ± 2.0	0.23	T _A *
76158.375	C ₄ H	8–7	4.00 ± 2.0	0.25	T _A *
76338.016	¹³ CCCN	8–7	7.00 ± 1.9	0.48	T _A *
77214.359	HC ₅ N	29–28	9.00 ± 2.2	0.61	T _A *
79160.367	C ₃ N	8–7	5.00 ± 1.6	0.76	T _A *
79876.710	HC ₅ N	30–29	8.00 ± 1.4	0.66	T _A *
80082.377	HC ₇ N	71–70	3.00 ± 1.4	0.19	T _A *
81505.202	CCS	6 ₇ –5 ₆	2.00 ± 1.0	0.20	T _A *
81534.111	HC ¹³ CCN	9–8	4.00 ± 1.1	0.26	T _A *
81881.462	HC ₃ N	9–8	100.00 ± 1.1	6.78	T _A *
82539.039	HC ₅ N	31–30	8.00 ± 1.1	0.64	T _A *
84746.165	³⁰ SiO	2–1	5.00 ± 0.9	0.34	T _A *
85201.346	HC ₅ N	32–31	8.00 ± 1.0	0.59	T _A *
85338.900	C ¹³ CH	2 _{1,2} –1 _{0,1}	5.00 ± 1.0	0.36	T _A *
85634.039	C ₄ H	9–8	5.00 ± 0.9	0.38	T _A *
85674.672	C ₄ H	9–8	5.00 ± 0.9	0.41	T _A *
85759.194	²⁹ SiO	3–2	7.00 ± 1.0	0.49	T _A *
86339.921	H ¹³ CN	1–0	57.00 ± 1.2	4.00	T _A *
86846.986	SiO	2–1	98.00 ± 1.0	6.38	T _A *
87284.105	CCH	1–0(3/2–1/2)	5.00 ± 1.0	0.36	T _A *
87316.898	CCH	1–0(3/2–1/2)	46.00 ± 1.0	3.87	T _A *
87328.585	CCH	1–0(3/2–1/2)	23.00 ± 1.0	1.64	T _A *
87401.989	CCH	1–0(1/2–1/2)	24.00 ± 1.0	1.98	T _A *
87407.165	CCH	1–0(1/2–1/2)	8.00 ± 1.0	0.67	T _A *
87446.470	CCH	1–0(1/2–1/2)	4.00 ± 1.0	0.36	T _A *
87863.630	HC ₅ N	33–32	7.00 ± 1.0	0.59	T _A *
88166.794	H ¹³ CCCN	10–9	1.00 ± 1.1	0.21	T _A *
88631.602	HCN	1–0	863.00 ± 17.5	54.94	T _A *
89054.953	C ₃ N	9–8	7.00 ± 1.1	1.09	T _A *
90525.889	HC ₅ N	34–33	6.00 ± 0.9	0.53	T _A *
90593.045	HCC ¹³ CN	10–9	3.00 ± 1.0	0.25	T _A *
90663.563	HNC	1–0	37.00 ± 1.1	3.04	T _A *
90771.566	SiS	5–4	9.00 ± 0.9	0.75	T _A *
90978.989	HC ₃ N	10–9	95.00 ± 1.1	7.14	T _A *
91979.994	CH ₃ CN	5 ₂ –4 ₂	3.00 ± 1.2	0.25	T _A *
92494.271	¹³ CS	2–1	4.00 ± 1.1	0.37	T _A *
93063.623	SiC ₂	4 _{0,4} –3 _{0,3}	20.00 ± 1.1	1.58	T _A *
93188.125	HC ₅ N	35–34	6.00 ± 1.0	0.45	T _A *
93870.091	CCS	7 ₈ –6 ₇	2.00 ± 1.0	0.20	T _A *
94245.355	SiC ₂	4 _{2,3} –3 _{2,2}	13.00 ± 1.2	1.14	T _A *
95150.414	C ₄ H	10–9(21/2–19/2)	6.00 ± 1.0	0.50	T _A *
95190.820	C ₄ H	10–9(19/2–17/2)	6.00 ± 1.0	0.48	T _A *
95579.416	SiC ₂	4 _{2,2} –3 _{2,1}	14.00 ± 1.1	1.14	T _A *
95850.335	HC ₅ N	36–35	6.00 ± 1.0	0.43	T _A *
96412.952	C ³⁴ S	2–1	16.00 ± 0.9	1.28	T _A *
96983.001	H ¹³ CCCN	11–10	2.00 ± 0.8	0.17	T _A *
97172.064	C ³³ S	2–1	3.00 ± 0.8	0.28	T _A *
97980.953	CS	2–1	264.00 ± 1.2	20.51	T _A *
98512.519	HC ₅ N	37–36	5.00 ± 0.7	0.48	T _A *
98949.383	C ₃ N	10–9	11.00 ± 0.8	2.00	T _A *
99661.467	HCC ¹³ CN	11–10	3.00 ± 0.8	0.31	T _A *
99866.503	CCS	8 ₇ –7 ₆	2.00 ± 0.8	0.16	T _A *
100076.385	HC ₃ N	11–10	114.00 ± 0.9	9.69	T _A *
101174.676	HC ₅ N	38–37	4.00 ± 0.8	0.44	T _A *
103836.806	HC ₅ N	39–38	4.00 ± 1.4	0.38	T _A *

Table A.1: continued.

104666.586	C ₄ H	11–10(23/2–21/2)	7.00 ± 1.5	0.66	T _A [*]
104706.867	C ₄ H	11–10(21/2–19/2)	7.00 ± 1.5	0.66	T _A [*]
106347.731	CCS	8 ₉ –7 ₈	3.00 ± 1.4	0.22	T _A [*]
106498.908	HC ₅ N	40–39	3.00 ± 1.5	0.36	T _A [*]
108647.523	¹³ CN	1 _{*,1,*} –0 _{1/2,*,*}	2.00 ± 1.8	0.30	T _A [*]
108721.003	HCC ¹³ CN	12–11	3.00 ± 1.2	0.27	T _A [*]
108784.203	¹³ CN	1 _{1,3/2,2,*} –0 _{1/2,1,*}	2.70 ± 1.8	0.31	T _A [*]
108843.633	C ₃ N	11–10	11.00 ± 1.8	1.64	T _A [*]
108924.303	SiS	6–5	16.00 ± 1.6	1.55	T _A [*]
109173.637	HC ₃ N	12–11	85.00 ± 1.9	7.86	T _A [*]
109218.148	¹³ CN	1 _{1/2,1,*} –0 _{1/2,0,1}	1.50 ± 1.8	0.09	T _A [*]
110201.354	¹³ CO	1–0	8.00 ± 2.2	1.40	T _A [*]
110383.499	CH ₃ CN	6 ₀ –5 ₀	4.00 ± 1.8	0.44	T _A [*]
111823.024	HC ₅ N	42–41	4.00 ± 1.6	0.40	T _A [*]
113168.781	CN	1 _{1/2} –0 _{1/2}	50.00 ± 2.1	2.97	T _A [*]
113496.430	CN	1 _{3/2} –0 _{1/2}	179.00 ± 2.1	4.71	T _A [*]
113659.508	U	–	10.00 ± 2.3	0.73	T _A [*]
114182.531	C ₄ H	12–11(25/2–23/2)	9.00 ± 2.9	0.90	T _A [*]
114221.023	C ₄ H	12–11(23/2–21/2)	11.00 ± 2.9	0.99	T _A [*]
114318.532	C ₈ H [–]	98–97	8.00 ± 2.7	0.17	T _A [*]
115271.202	CO	1–0	549.00 ± 26.7	67.18	T _A [*]
115382.377	SiC ₂	5 _{0,5} –4 _{0,4}	32.00 ± 3.7	3.46	T _A [*]
199812.375	C ₄ H	21–20(43/2–41/2)	14.00 ± 4.5	0.90	T _A [*]
199826.156	C ₄ H v7	21 _{–1,41/2} –20 _{1,39/2}	8.00 ± 4.5	0.64	T _A [*]
199850.781	C ₄ H	21–20(41/2–39/2)	18.00 ± 4.5	1.35	T _A [*]
200135.388	HC ₃ N	22–21	42.00 ± 4.3	2.47	T _A [*]
200162.407	SiC ₂	9 _{0,9} –8 _{0,8}	58.00 ± 4.3	3.46	T _A [*]
202355.507	CH ₃ CN	11 ₀ –10 ₀	7.00 ± 4.7	0.37	T _A [*]
207772.172	C ₃ N	21–20	9.00 ± 3.0	0.69	T _A [*]
207851.962	²⁹ Si ³⁴ S	12–11	9.00 ± 3.0	0.60	T _A [*]
207867.625	U	–	9.00 ± 3.0	0.69	T _A [*]
209230.199	HC ₃ N	23–22	23.00 ± 6.2	1.52	T _A [*]
209324.906	C ₄ H	22–21(45/2–43/2)	11.00 ± 5.5	0.93	T _A [*]
209363.297	C ₄ H	22–21(43/2–41/2)	15.00 ± 5.5	1.13	T _A [*]
209891.991	SiC ₂	9 _{2,8} –8 _{2,7}	39.00 ± 5.3	2.42	T _A [*]
211023.281	SiC ₂	9 _{8,2} –8 _{8,1}	10.00 ± 4.8	0.50	T _A [*]
211853.467	³⁰ SiO	5–4	21.00 ± 5.4	1.34	T _A [*]
212031.873	SiC ₂	9 _{6,4} –8 _{6,3}	24.00 ± 5.5	1.42	T _A [*]
213208.022	SiC ₂	9 _{4,6} –8 _{4,5}	28.00 ± 4.9	1.88	T _A [*]
213292.328	SiC ₂	9 _{4,5} –8 _{4,4}	24.00 ± 4.9	1.49	T _A [*]
214385.752	²⁹ SiO	5–4	28.00 ± 6.7	1.58	T _A [*]
217104.920	SiO	5–4	403.00 ± 3.4	21.01	T _A [*]
217297.125	¹³ CN	2–1(3/2–1/2)	2.00 ± 2.1	0.21	T _A [*]
217456.594	¹³ CN	2–1(5/2–3/2)	4.00 ± 2.1	0.31	T _A [*]
217663.203	C ₃ N	22–21	4.00 ± 2.1	0.32	T _A [*]
217817.656	SiS	12–11	76.00 ± 4.7	5.04	T _A [*]
218007.543	SiN	5–4(9/2–7/2)	7.00 ± 3.6	0.52	T _A [*]
218324.709	HC ₃ N	24–23	24.00 ± 3.5	1.69	T _A [*]
218512.915	SiN	5–4(11/2–9/2)	10.00 ± 3.6	0.67	T _A [*]
218837.000	C ₄ H	23–22(47/2–45/2)	13.00 ± 3.8	0.77	T _A [*]
218875.344	C ₄ H	23–22(45/2–43/2)	13.00 ± 3.8	1.01	T _A [*]
220398.684	¹³ CO	2–1	20.00 ± 4.1	2.35	T _A [*]
220747.259	CH ₃ CN	12 ₀ –11 ₀	10.00 ± 3.6	1.05	T _A [*]
220773.676	SiC ₂	10 _{0,10} –9 _{0,9}	34.00 ± 3.6	2.48	T _A [*]
222009.399	SiC ₂	9 _{2,7} –8 _{2,6}	43.00 ± 3.9	2.81	T _A [*]
224692.531	U	–	10.00 ± 3.4	0.74	T _A [*]
225554.609	CH ₂ NH	1 _{1,1} –0 _{0,0}	5.00 ± 2.1	0.28	T _A [*]
226333.094	CN	2–1(3/2–3/2)	24.00 ± 3.4	2.80	T _A [*]
226658.922	CN	2–1(3/2–1/2)	103.00 ± 3.0	5.70	T _A [*]
226876.453	CN	2–1(5/2–3/2)	240.00 ± 2.9	10.40	T _A [*]
227418.906	HC ₃ N	25–24	22.00 ± 3.6	1.61	T _A [*]

Table A.1: continued.

228348.594	C ₄ H	24–23(49/2–47/2)	10.00 ± 2.9	0.77	T _A [*]
228386.953	C ₄ H	24–23(47/2–45/2)	12.00 ± 2.9	0.97	T _A [*]
228557.844	C ₄ H v7	24–23	4.00 ± 1.8	0.55	T _A [*]
230463.712	U	–	404.00 ± 8.9	0.54	T _A [*]
230538.000	CO	2–1	1540.00 ± 47.5	113.97	T _A [*]
231220.685	¹³ CS	5–4	16.00 ± 10.9	0.99	T _A [*]
232534.063	SiC ₂	10 _{2,9} –9 _{2,8}	28.00 ± 8.9	2.08	T _A [*]
235961.366	SiS	13–12	68.00 ± 9.9	4.70	T _A [*]
236512.776	HC ₃ N	26–25	19.00 ± 8.4	1.22	T _A [*]
236962.031	U	–	16.00 ± 7.7	0.94	T _A [*]
237150.009	SiC ₂	10 _{4,7} –9 _{4,6}	29.00 ± 8.7	2.20	T _A [*]
237331.303	SiC ₂	10 _{4,6} –9 _{4,5}	18.00 ± 5.7	1.40	T _A [*]
237859.688	C ₄ H	25–24(51/2–49/2)	3.00 ± 4.0	0.43	T _A [*]
237898.031	C ₄ H	25–24(49/2–47/2)	4.00 ± 4.0	0.38	T _A [*]
239073.047	U	–	49.00 ± 3.4	1.76	T _A [*]
239098.406	U	–	57.00 ± 3.4	1.73	T _A [*]
241016.089	C ³⁴ S	5–4	60.00 ± 3.8	4.24	T _A [*]
241367.704	SiC ₂	11 _{0,11} –10 _{0,10}	33.00 ± 3.5	2.43	T _A [*]
242913.610	C ³³ S	5–4	13.00 ± 3.7	0.96	T _A [*]
244935.555	CS	5–4	879.00 ± 4.6	51.10	T _A [*]
245606.307	HC ₃ N	27–26	14.00 ± 3.0	1.15	T _A [*]
247529.132	SiC ₂	10 _{2,8} –9 _{2,7}	46.00 ± 6.2	3.20	T _A [*]
254103.212	SiS	14–13	53.00 ± 4.8	3.95	T _A [*]
254216.652	³⁰ SiO	6–5	17.00 ± 4.7	1.28	T _A [*]
254699.486	HC ₃ N	28–27	19.00 ± 5.0	1.59	T _A [*]
254981.478	SiC ₂	11 _{2,10} –10 _{2,9}	23.00 ± 4.6	1.67	T _A [*]
257255.213	²⁹ SiO	6–5	24.00 ± 5.1	1.83	T _A [*]
258065.049	SiC ₂	11 _{8,(4–3)} –10 _{8,(3–2)}	8.00 ± 5.6	0.50	T _A [*]
259011.798	H ¹³ CN	3–2	179.00 ± 5.1	11.80	T _A [*]
259433.413	SiC ₂	11 _{6,5} –10 _{6,4}	16.00 ± 4.9	1.22	T _A [*]
260518.018	SiO	6–5	277.00 ± 6.2	17.65	T _A [*]
261150.699	SiC ₂	11 _{4,8} –10 _{4,7}	12.00 ± 6.0	0.98	T _A [*]
261509.322	SiC ₂	11 _{4,7} –10 _{4,6}	15.00 ± 5.5	1.12	T _A [*]
261978.120	CCH	3 _{7/2,3} –2 _{5/2,3}	21.00 ± 5.7	1.19	T _A [*]
262004.260	CCH	3 _{7/2,4} –2 _{5/2,3}	244.00 ± 5.7	23.22	T _A [*]
262006.482	CCH	3 _{7/2,3} –2 _{5/2,2}	293.00 ± 5.7	18.69	T _A [*]
262064.986	CCH	3 _{5/2,3} –2 _{3/2,2}	237.00 ± 5.7	21.51	T _A [*]
262067.469	CCH	3 _{5/2,2} –2 _{3/2,1}	150.00 ± 5.7	9.71	T _A [*]
262078.934	CCH	3 _{5/2,2} –2 _{3/2,1}	41.00 ± 5.7	2.38	T _A [*]
262208.614	CCH	3 _{5/2,3} –2 _{5/2,3}	9.00 ± 9.6	1.19	T _A [*]
262222.585	CCH	3 _{5/2,2} –2 _{5/2,3}	5.00 ± 9.6	0.34	T _A [*]
262236.958	CCH	3 _{5/2,3} –2 _{5/2,2}	0.00 ± 9.6	0.39	T _A [*]
262250.929	CCH	3 _{5/2,2} –2 _{5/2,2}	0.00 ± 9.6	0.32	T _A [*]
265886.433	HCN	3–2	1759.00 ± 19.2	101.93	T _A [*]
268479.867	U	–	26.00 ± 3.5	1.04	T _A [*]
271981.107	HNC	3–2	53.00 ± 13.2	4.58	T _A [*]
272243.053	SiS	15–14	57.00 ± 11.4	4.03	T _A [*]
272787.823	SiC ₂	11 _{2,9} –10 _{2,8}	27.00 ± 15.0	2.48	T _A [*]
556936.002	H ₂ O	1 _{1,0} –1 _{0,1}	28.00 ± 3.0	1.26	T _{mb}
572498.160	NH ₃	1 _{0,1} –0 _{0,–1}	22.00 ± 2.4	1.33	T _{mb}
690552.086	H ¹³ CN	8–7	9.00 ± 5.5	0.60	T _{mb}
691473.076	CO	6–5	156.00 ± 5.8	8.51	T _{mb}
694294.129	SiO	16–15	12.00 ± 5.6	0.98	T _{mb}
1113342.964	H ₂ O	1 _{1,1} –0 _{0,0}	35.00 ± 12.1	1.87	T _{mb}
1151449.090	HCN	13–12	112.00 ± 29.7	4.19	T _{mb}
1151985.444	CO	10–9	170.00 ± 24.3	8.61	T _{mb}
1841345.514	CO	16–15	155.24 ± 46.6	7.72	T _{mb}

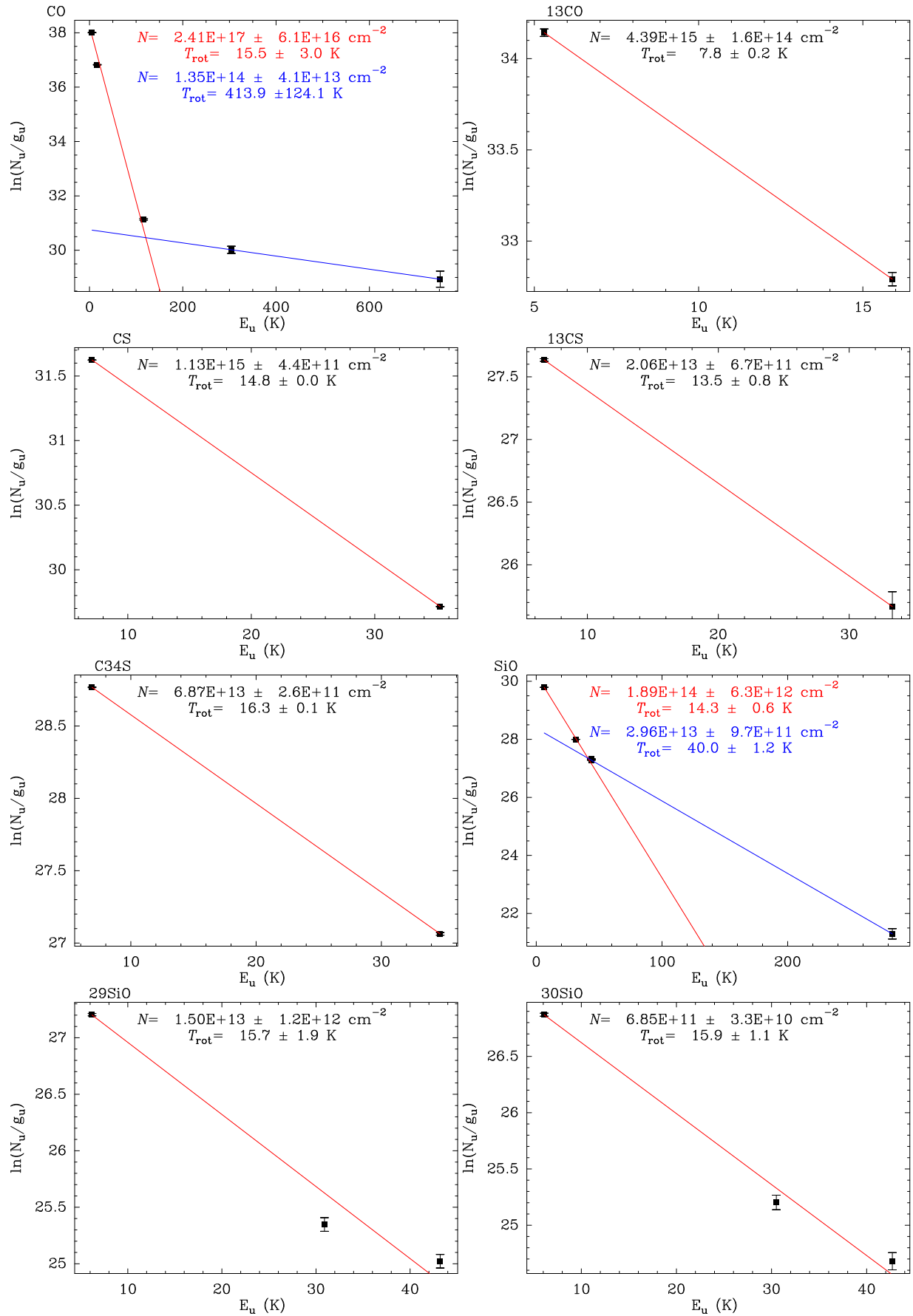


Fig. B.1: Results of the rotational diagram fitting I.

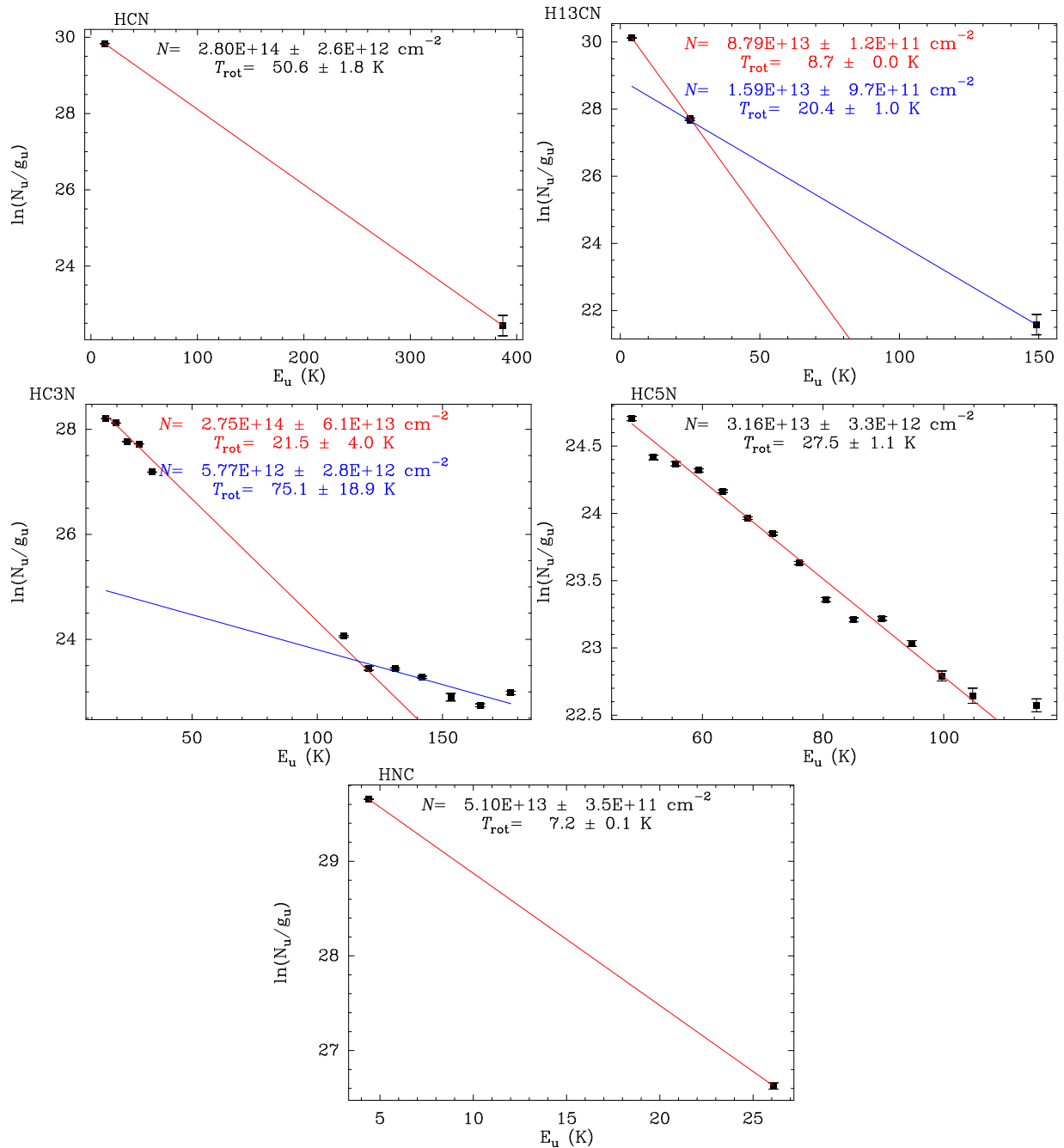


Fig. B.2: Results of the rotational diagram fitting II.

Appendix B: Rotational Diagrams

Appendix C: Molecular line maps

Appendix D: Spectral line survey

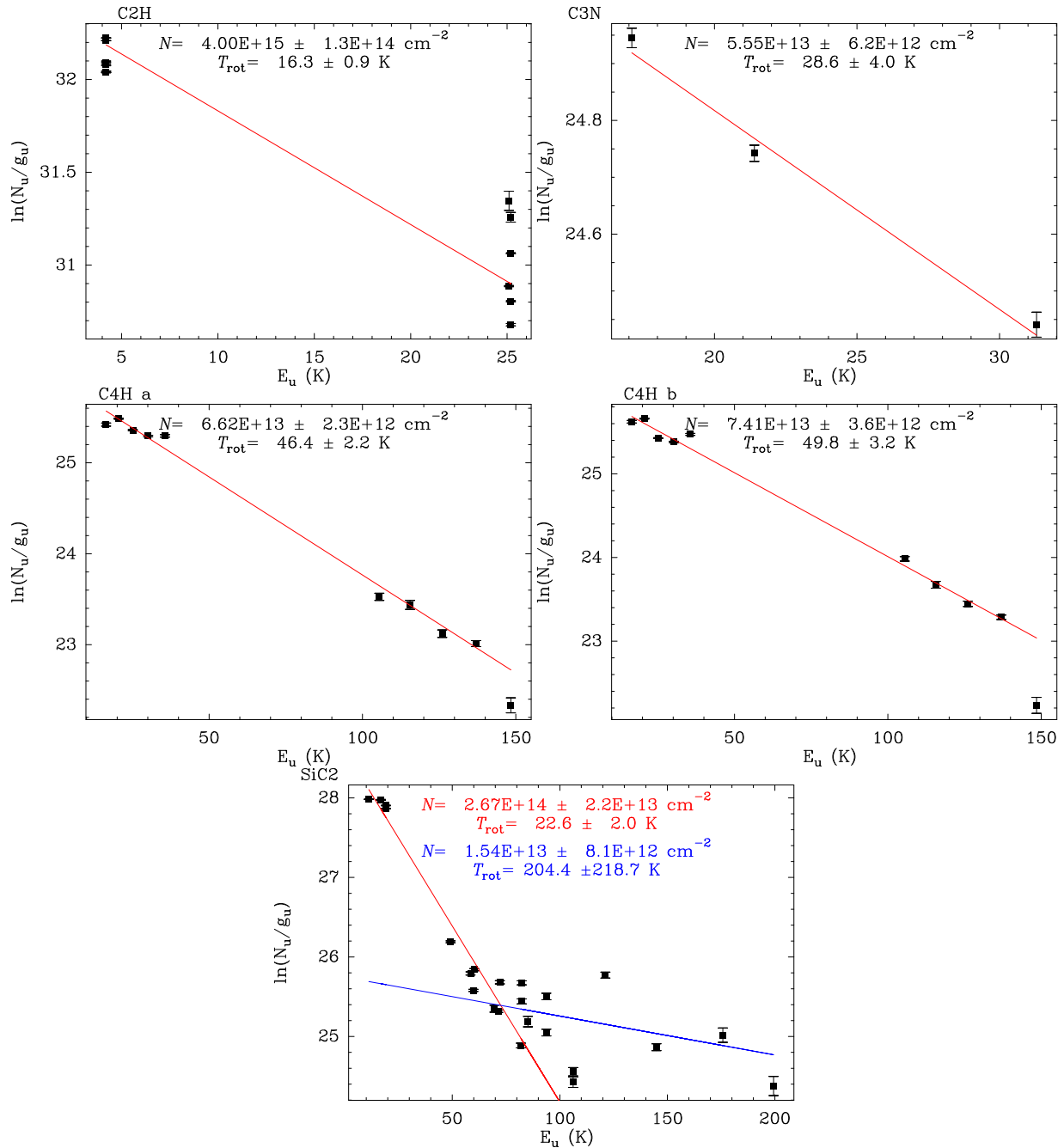


Fig. B.3: Results of the rotational diagram fitting III.

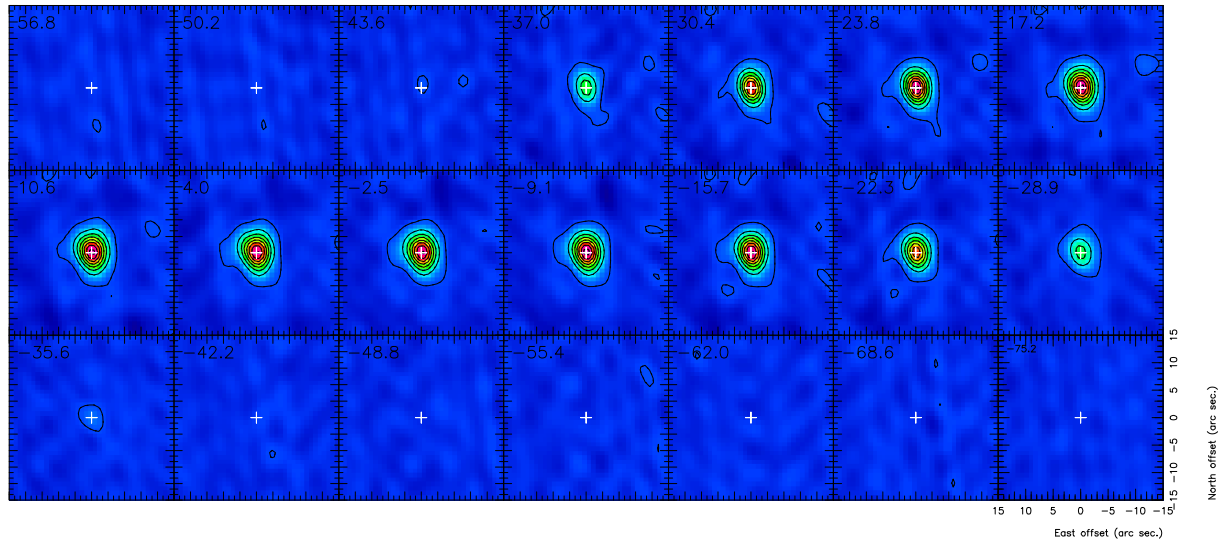


Fig. C.1: Molecular channel map of SiO 2-1. HPBW = $4''.35 \times 2''.84$. Level step is 20σ , being $\sigma = 2.39$ mJy/beam and the first contour at 3σ .

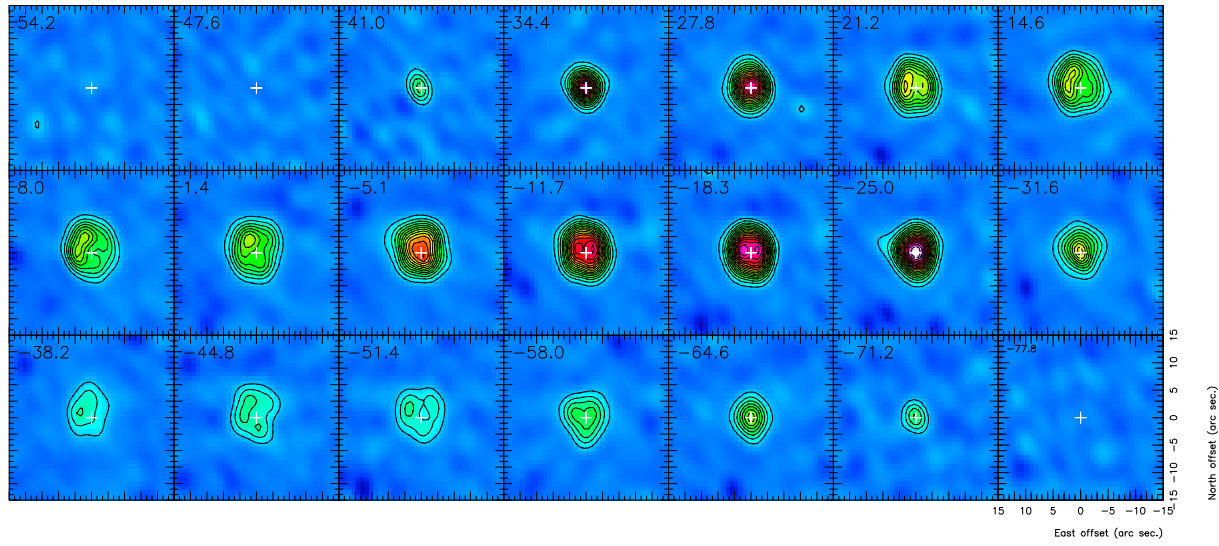


Fig. C.2: Molecular channel map of C₂H. HPBW = $4''.32 \times 2''.82$. Level step is 3σ , being $\sigma = 1.85$ mJy/beam and the first contour at 3σ .

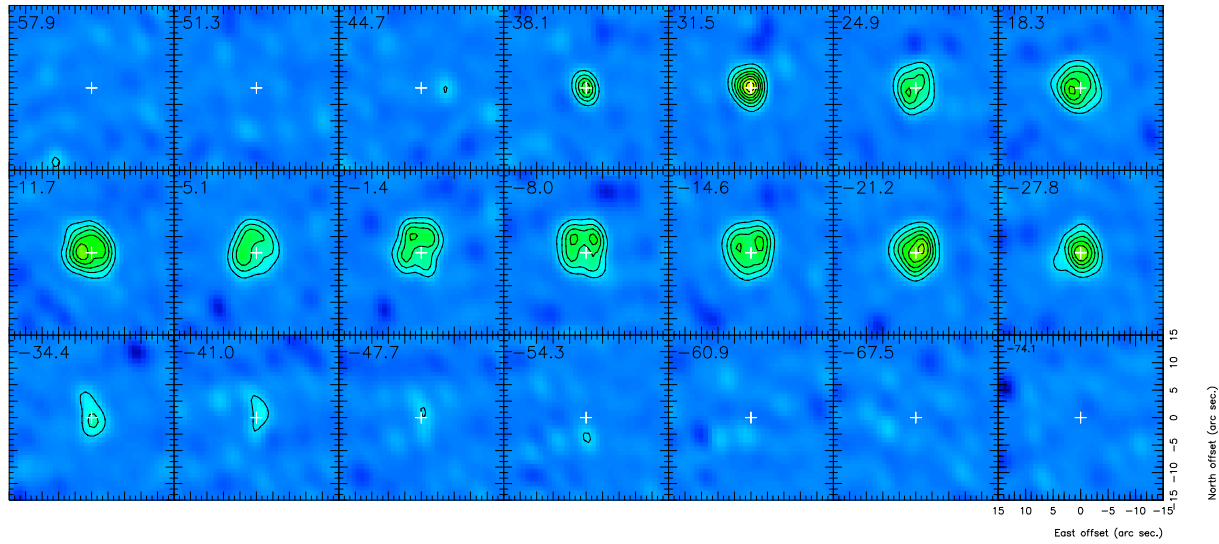


Fig. C.3: Molecular channel map of C₂H. HPBW = 4''.31 × 2''.82. Level step is 3 σ , being $\sigma = 2.22$ mJy/beam and the first contour at 3 σ .

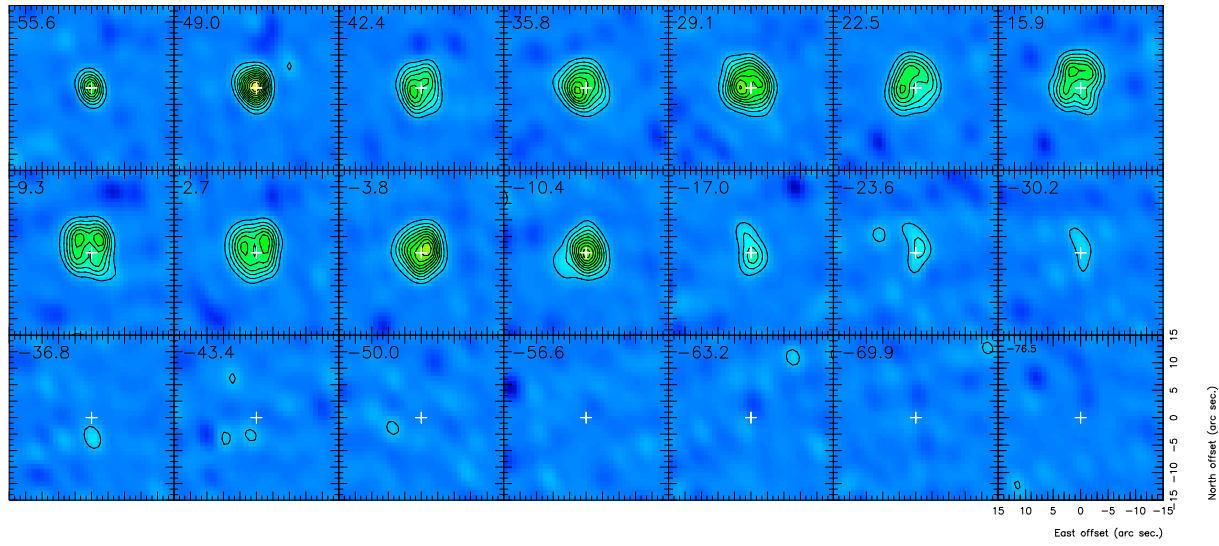


Fig. C.4: Molecular channel map of C₂H. HPBW = 4''.36 × 2''.83. Level step is 3 σ , being $\sigma = 1.43$ mJy/beam and the first contour at 3 σ .

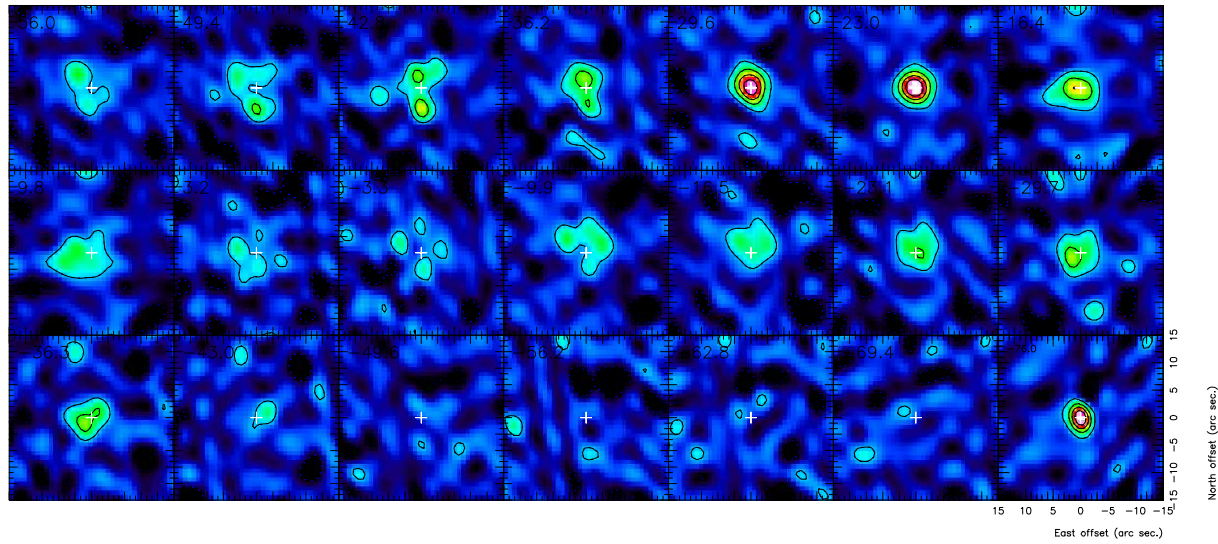


Fig. C.5: Molecular channel map of C_3N . HPBW = $4.^{\prime\prime}25 \times 2.^{\prime\prime}78$. Level step is 3σ , being $\sigma = 1.48 \text{ mJy/beam}$ and the first contour at 3σ .

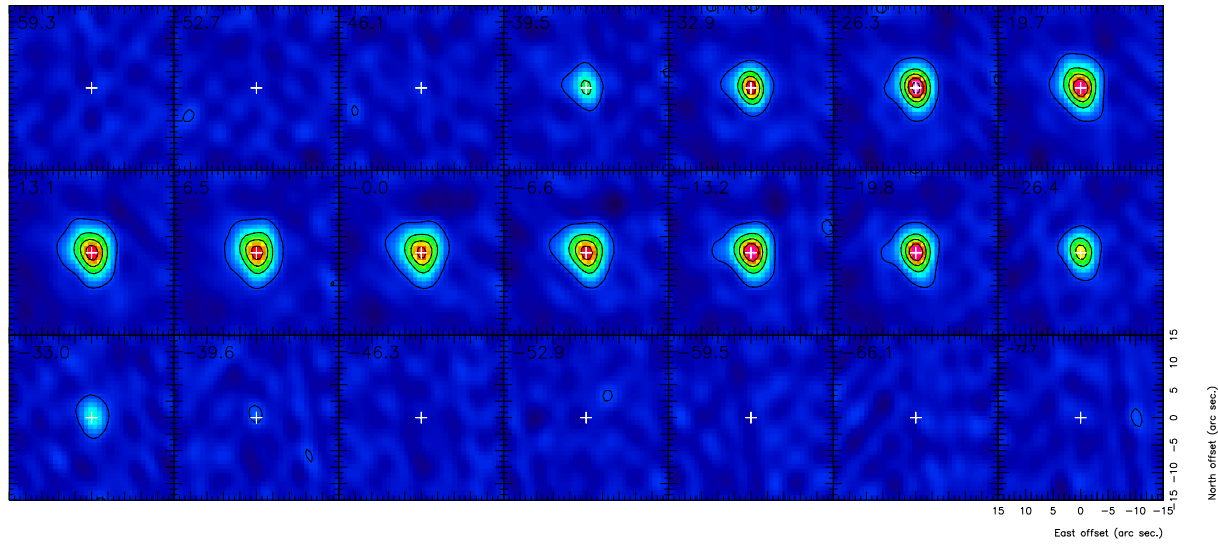


Fig. C.6: Molecular channel map of H^{13}CN . HPBW = $4.^{\prime\prime}37 \times 2.^{\prime\prime}86$. Level step is 20σ , being $\sigma = 2.13 \text{ mJy/beam}$ and the first contour at 3σ .

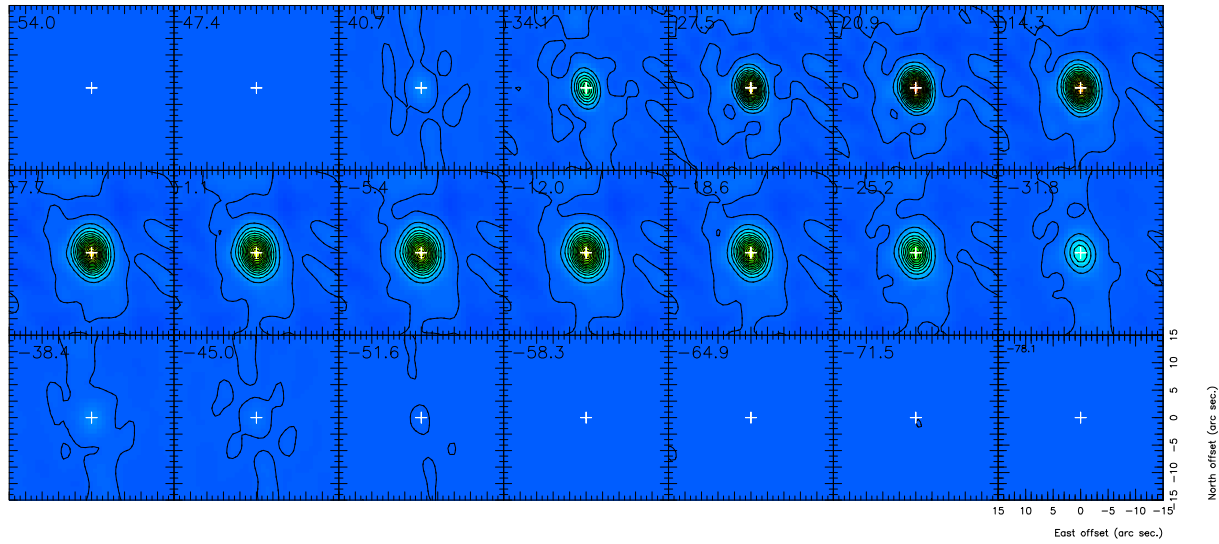


Fig. C.7: Molecular channel map of HCN. HPBW = $4.^{\prime\prime}27 \times 2.^{\prime\prime}79$. Level step is 100σ , being $\sigma = 2.22$ mJy/beam and the first contour at 3σ .

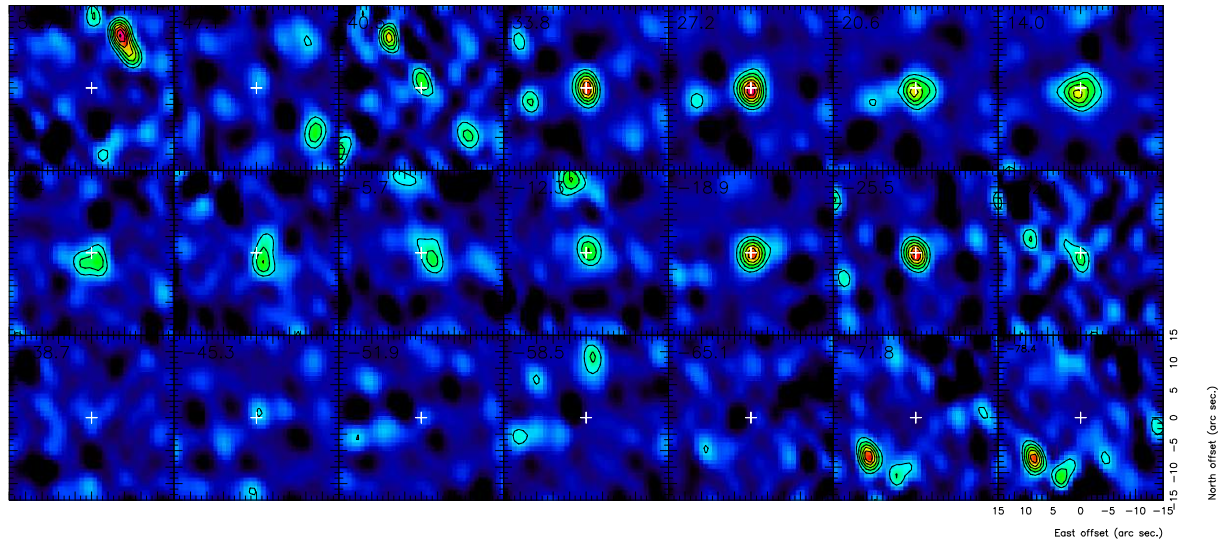


Fig. C.8: Molecular channel map of HC₅N. HPBW = $4.^{\prime\prime}31 \times 2.^{\prime\prime}82$. Level step is 2σ , being $\sigma = 1.41$ mJy/beam and the first contour at 3σ .

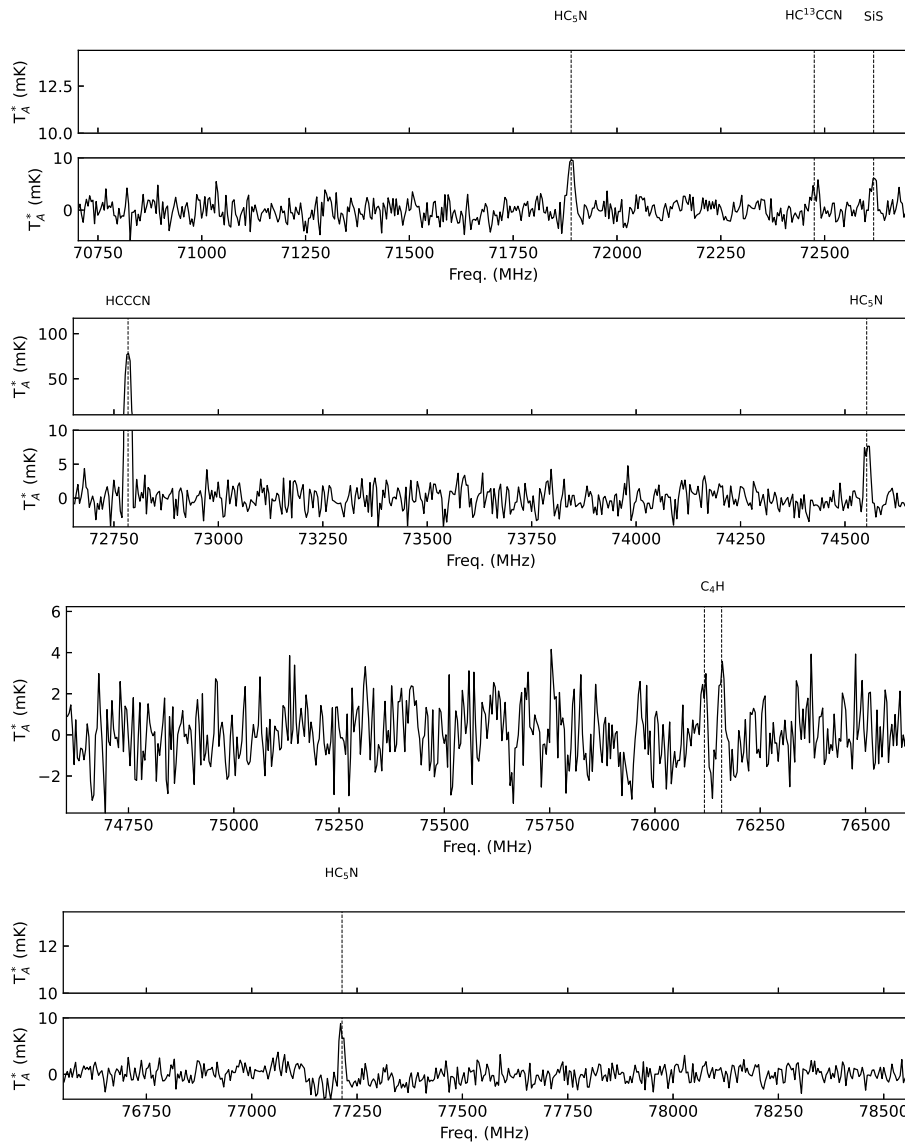


Fig. D.1: Spectral survey obtained with the IRAM 30m telescope at the atmospheric window of 3 mm.

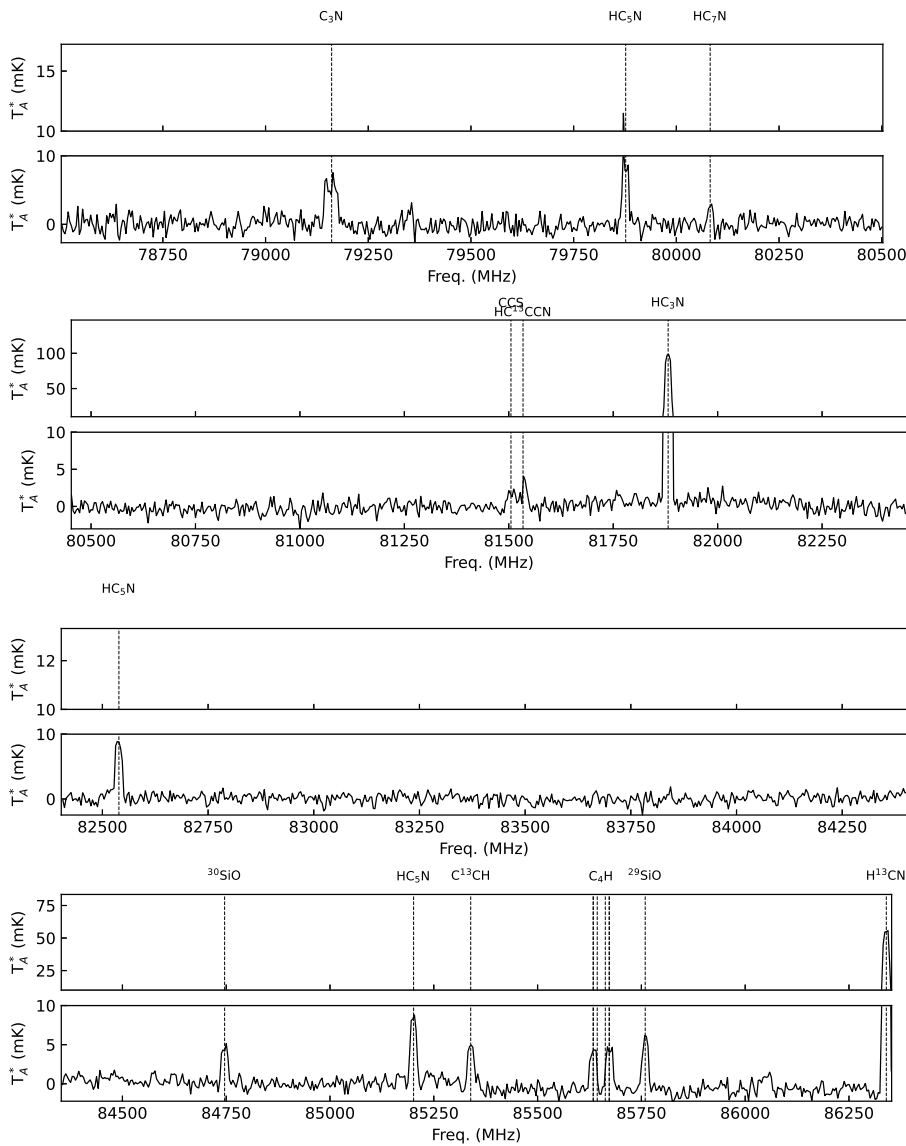


Fig. D.1: Spectral survey obtained with the IRAM 30m telescope at the atmospheric window of 3 mm. (continued)

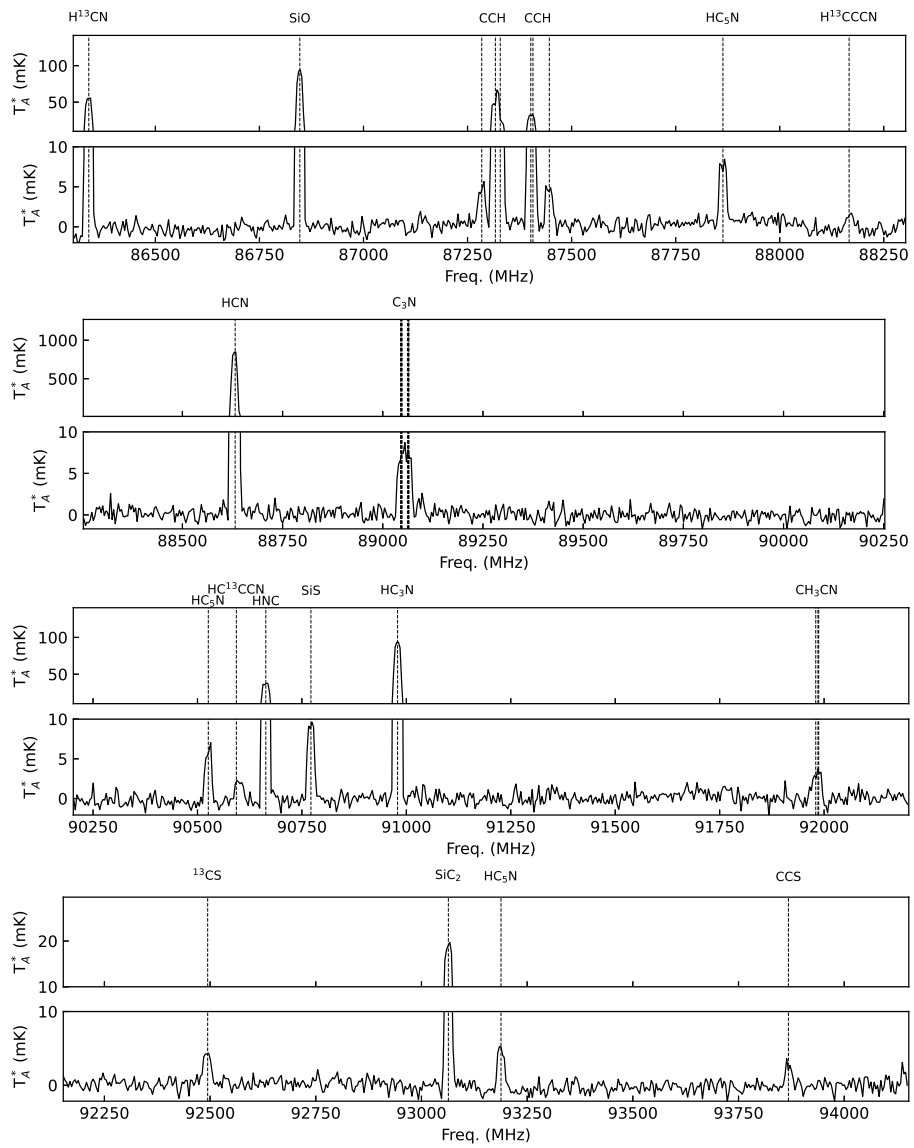


Fig. D.1: Spectral survey obtained with the IRAM 30m telescope at the atmospheric window of 3 mm. (continued)

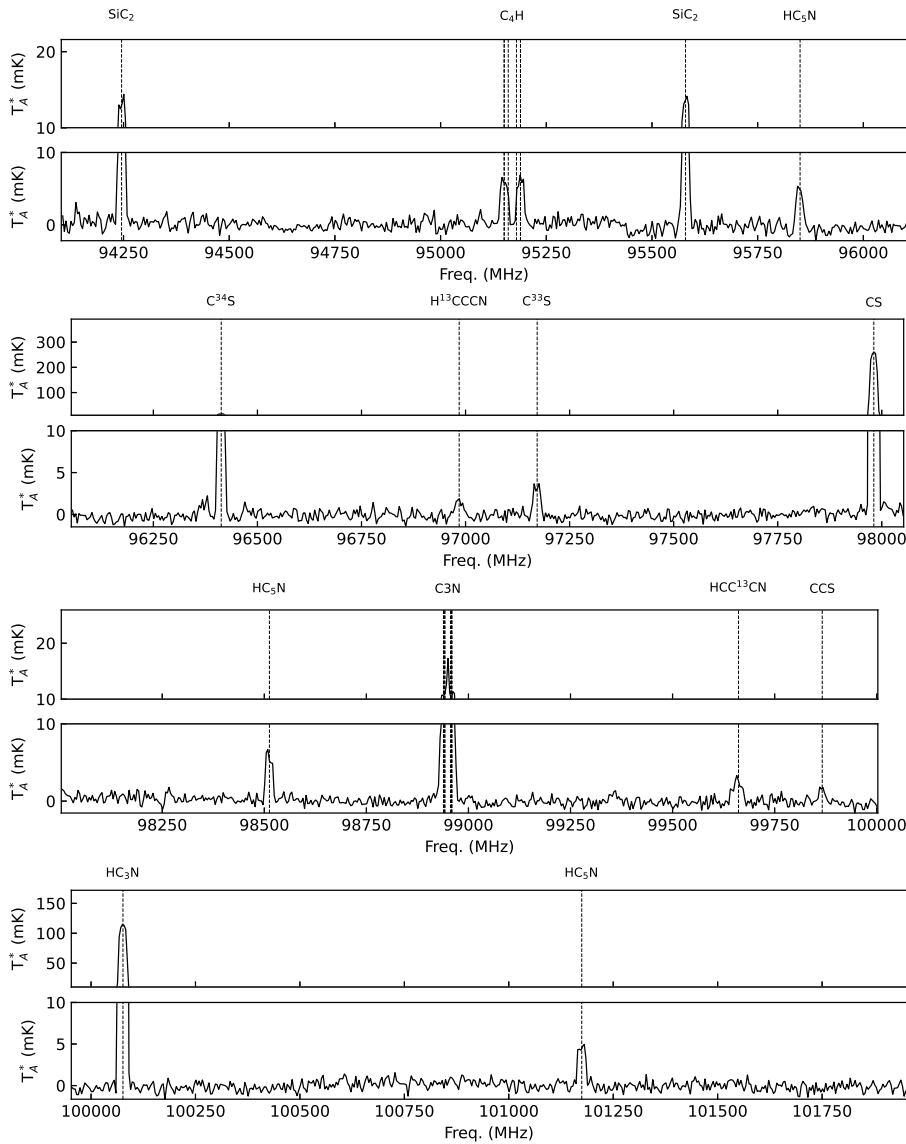


Fig. D.1: Spectral survey obtained with the IRAM 30m telescope at the atmospheric window of 3 mm. (continued)

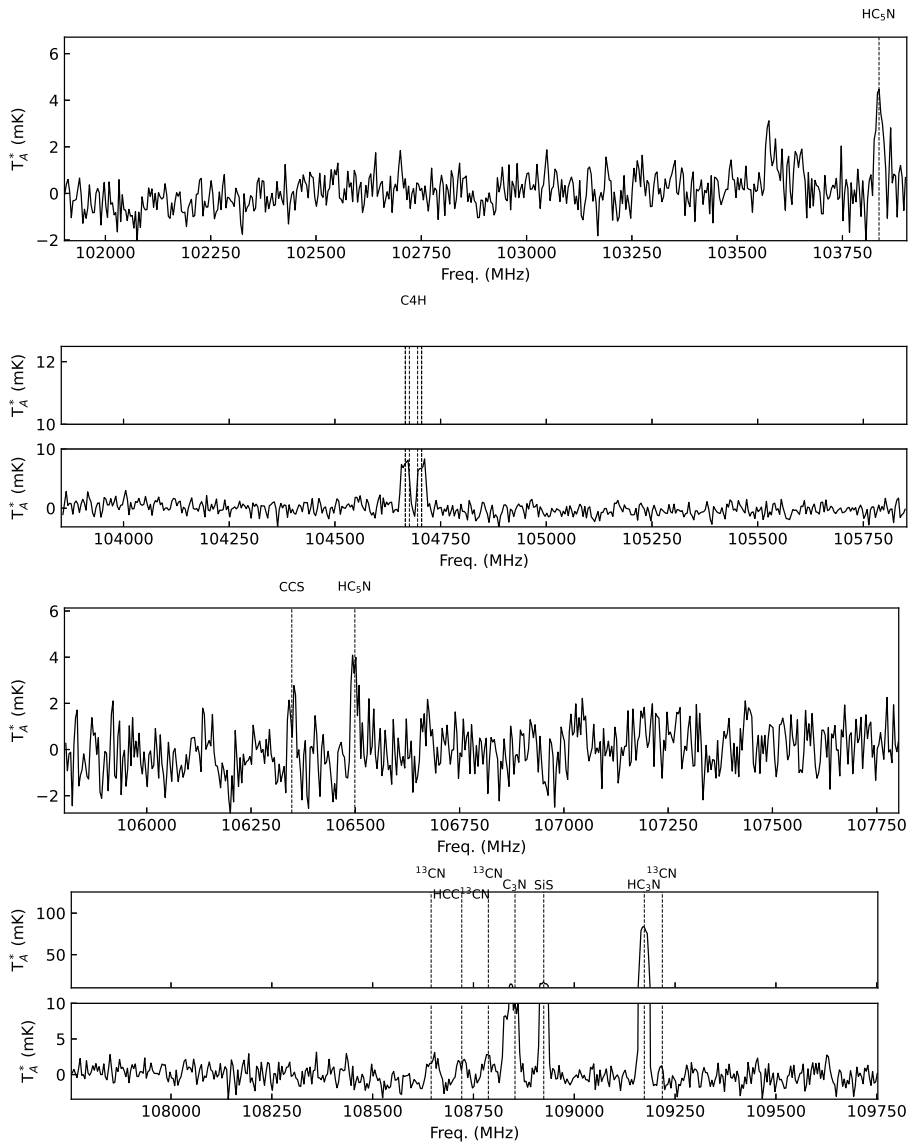


Fig. D.1: Spectral survey obtained with the IRAM 30m telescope at the atmospheric window of 3 mm. (continued)

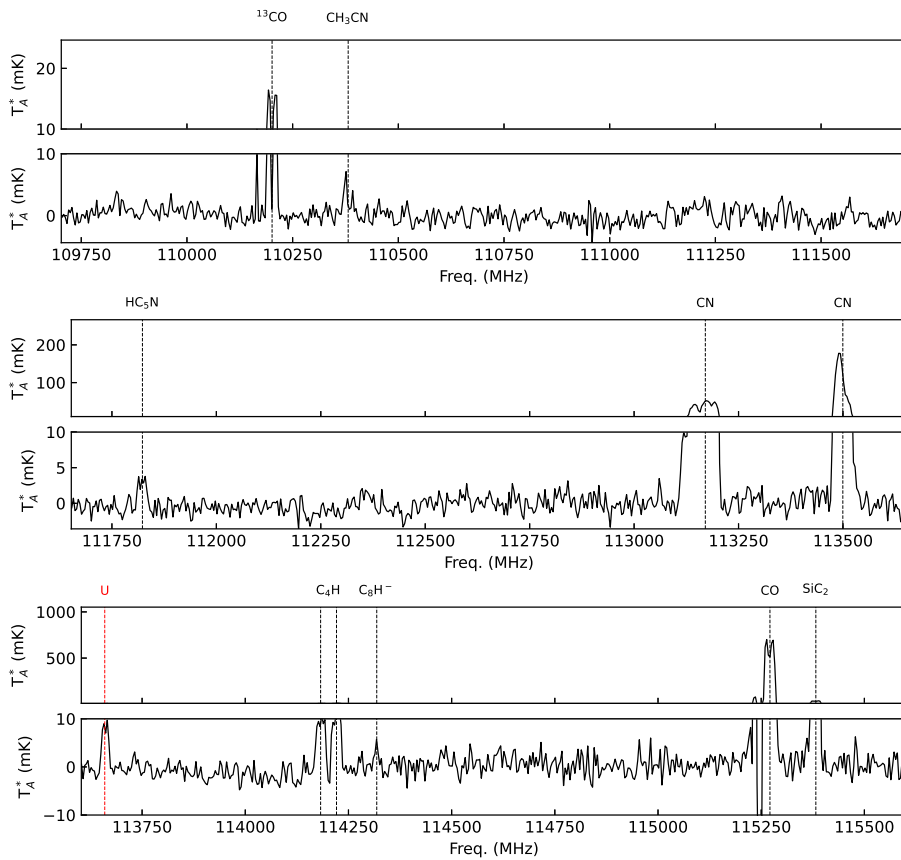


Fig. D.1: Spectral survey obtained with the IRAM 30m telescope at the atmospheric window of 3 mm. (continued)

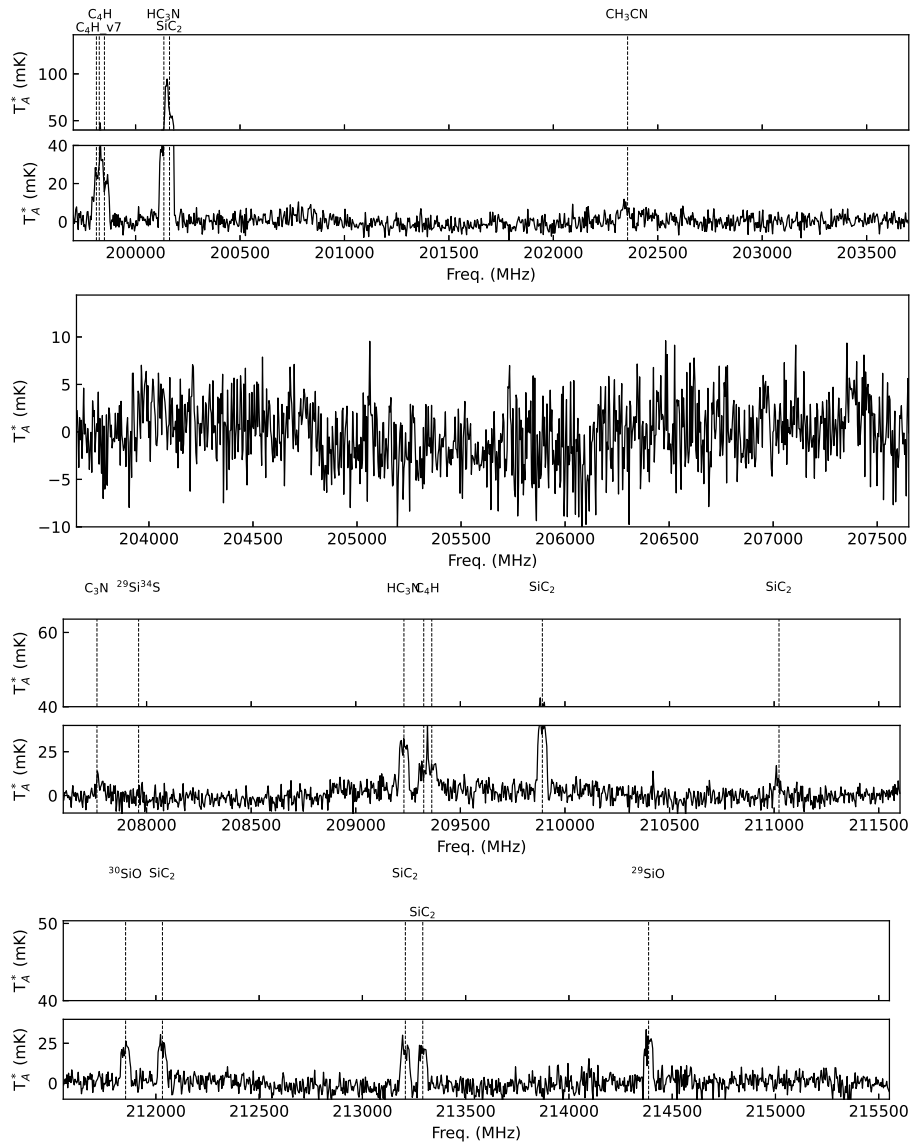


Fig. D.1: Spectral survey obtained with the IRAM 30m telescope at the atmospheric window of 1 mm.

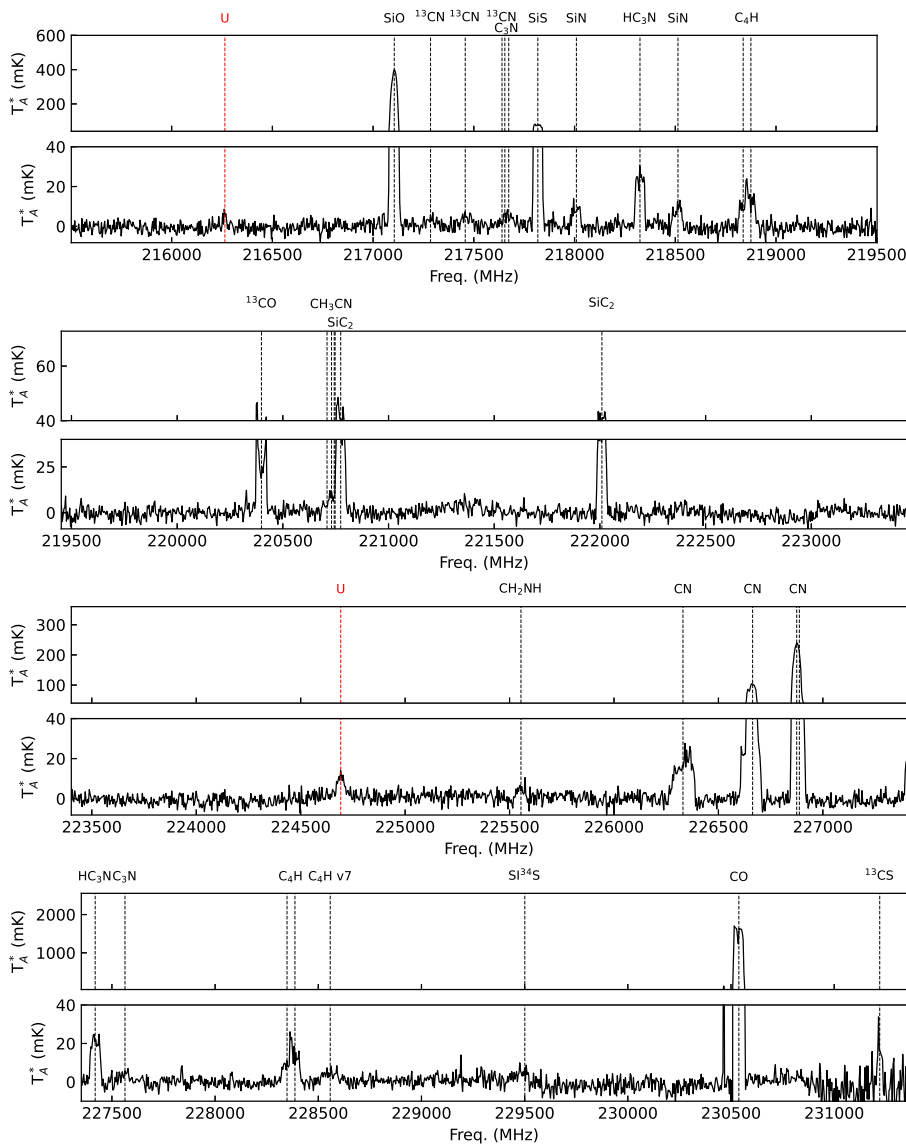


Fig. D.1: Spectral survey obtained with the IRAM 30m telescope at the atmospheric window of 1 mm. (continued)

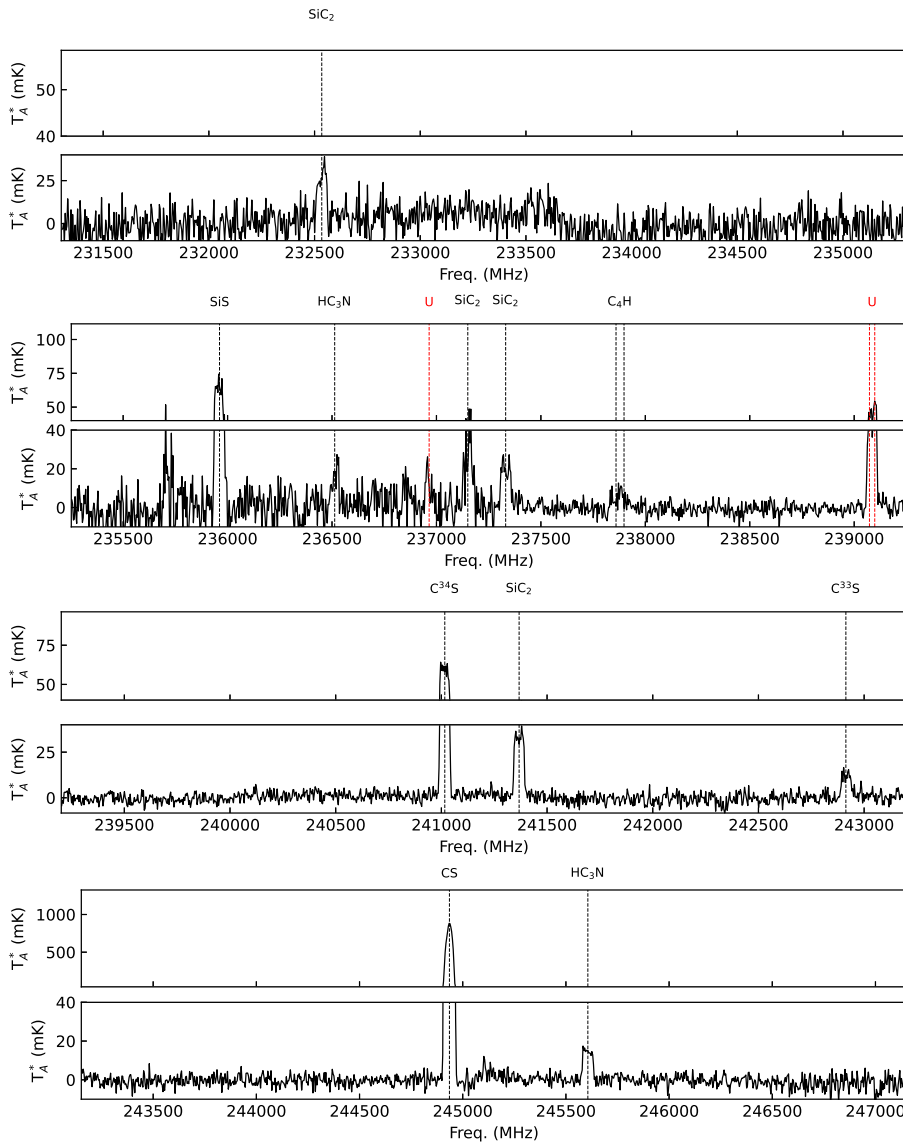


Fig. D.1: Spectral survey obtained with the IRAM 30m telescope at the atmospheric window of 1 mm. (continued)

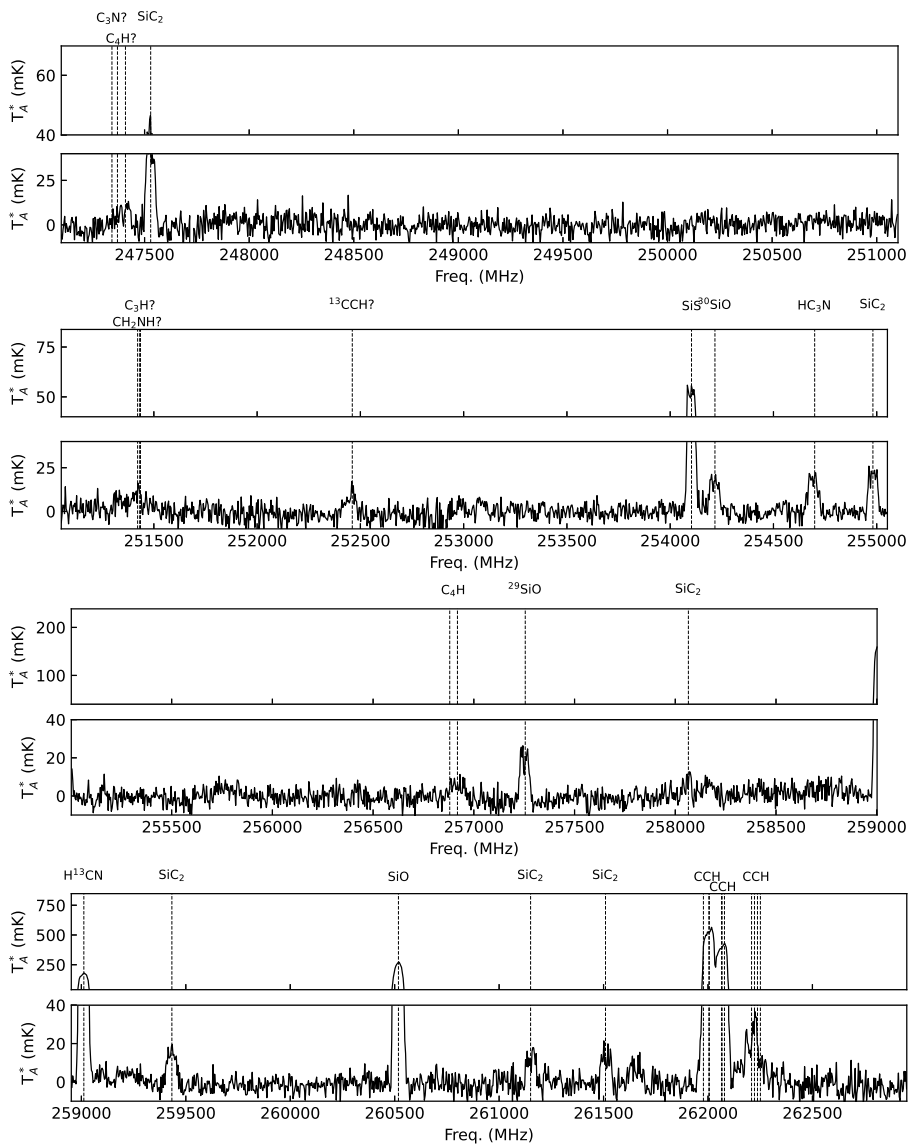


Fig. D.1: Spectral survey obtained with the IRAM 30m telescope at the atmospheric window of 1 mm. (continued)

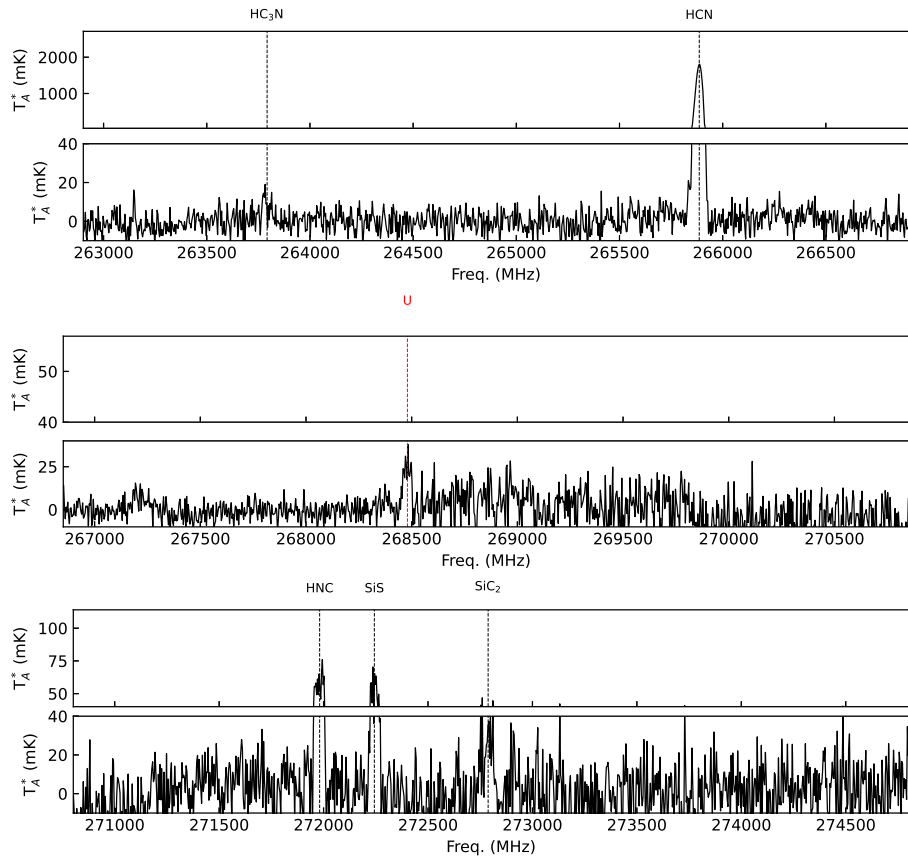


Fig. D.1: Spectral survey obtained with the IRAM 30m telescope at the atmospheric window of 1 mm. (continued)